www.advelectronicmat.de

Recent Advances in Bioresorbable Biomedical Applications: From Materials to Devices

Do Yun Park, Hye-Min Lee, Su-Hwan Kim, Youngmin Sim, Yoojin Kang, Gyu-rim Jang, Sara Kim, Kyeongha Kwon,* and Hanjun Ryu*

Wearable and implantable devices provide users with continuous monitoring and treatment, and bioresorbable features can facilitate the use of temporary biomedical devicesand reduce electronic wastes (e-wastes). Bioresorbable metals and polymers offer multiple benefits, such as high conductivity and mechanical support, for skin-interfaced and implantable biomedical devices in versatile biomedical applications. These materials dissolve naturally after their targeted lifetime, avoiding complications arising from retrieval surgeries and preventing e-waste accumulation. This review summarizes recent advances in both bioresorbable materials and devices, highlighting various polymers, semiconductors, and metal options along with their dissolution processes. The following contents introduce the current developments in bioresorbable skin-interfaced and implantable systems including electrostimulation (ES), energy harvesting, sensor, and transistor systems. A concluding section discusses current challenges and future research opportunities in this field.

D. Y. Park, S. Kim, K. Kwon Graduate School of Artificial Intelligence Semiconductor Korea Advanced Institute of Science and Technology Daejeon 34141, Republic of Korea E-mail: kyeongha@kaist.ac.kr

Department of Advanced Materials Engineering Chung-Ang University Anseong 17546, Republic of Korea

E-mail: hanjunryu@cau.ac.kr S.-H. Kim, Y. Sim, Y. Kang, G.-rim Jang, K. Kwon

S.-H. Kim, Y. Sim, Y. Kang, G.-rim Jang, K. Kwon School of Electrical Engineering Korea Advanced Institute of Science and Technology

Daejeon 34141, Republic of Korea H. Rvu

H.-M. Lee, H. Ryu

Department of Intelligence Energy and Industry Chung-Ang University Seoul 06974, Republic of Korea

The ORCID identification number(s) for the author(s) of this article can be found under https://doi.org/10.1002/aelm.202400997

© 2025 The Author(s). Advanced Electronic Materials published by Wiley-VCH GmbH. This is an open access article under the terms of the Creative Commons Attribution License, which permits use, distribution and reproduction in any medium, provided the original work is properly cited.

DOI: 10.1002/aelm.202400997

1. Introduction

Wearable or implantable medical devices aim to provide continuous monitoring, appropriate treatments, and feedback for users to modulate their lifestyles. Especially, wearable skin-interfaced systems which directly contact skin or wound site enable stimulation^[1-6] and biosignal monitoring.[7-16] Implantable medical devices powered by batteries, such as cardioverter defibrillators, pacemakers, and neurostimulators, provide patients with convenient medical benefits and change their lives.[17] As the world population and senior citizens are growing, the global implantable medical devices market is predicted to continuously grow from \$91.8 billion in 2020 to \$179 billion in 2030.[18] Bioresorbable (or equivalently bioabsorbable) materialsbased temporal skin-interfaced and implantable biomedical systems further extend the applications to cardiac pacing, [1]

transdermal drug delivery,^[5,6] physiological sensing,^[7–16] opioid, nerve stimulators, and wound regeneration.[2-4, 19-21] Compositions of organic and inorganic materials that chemically dissolve in biofluids facilitate sophisticated biomedical devices, which can bypass risks and costs associated with retrieval surgery after their intended operational timeline. Bioresorbable materials can also reduce electronic wastes (e-wastes) from biomedical devices through their natural dissolution properties. Bioresorbable metals (e.g., magnesium (Mg), molybdenum (Mo), iron (Fe), zinc (Zn), and tungsten (W) and bioresorbable polymers (e.g., polylactic acid (PLA), polyglycolic acid (PGA), poly(vinyl alcohol) (PVA), etc.) are well-established in hydrolysis reactions and dissolution processes (Figure 1).[22,23] Different rates of dissolution, levels of water penetration, and hydrophobicity determine the natural functional lifetime of bioresorbable devices, and mechanically, thermally, optically, or electrically triggered acceleration strategies suggest a controllable functional lifetime of devices.^[24] Passive bioresorbable systems, which are composed of strictly selected materials and designed structures, naturally resorb their components, gradually lose their performance, and rapidly lose their performance after the threshold functional lifetime of a weak component.^[25] Otherwise, active bioresorbable systems, which consist of materials with low dissolution rates, secure stable performance, and trigger dissolution on demand.[26]

ced.onlinelibrary.wiley.com/doi/10.1002/keln.2024/00997 by Chung-Ang University, Scoul, Wiley Online Library on [06/07/2025]. See the Terms and Conditions (htps://onlinelibrary.wiley.com/terms-and-conditions) on Wiley Online Library for rules of use; OA articles are governed by the applicable Creative Commons.

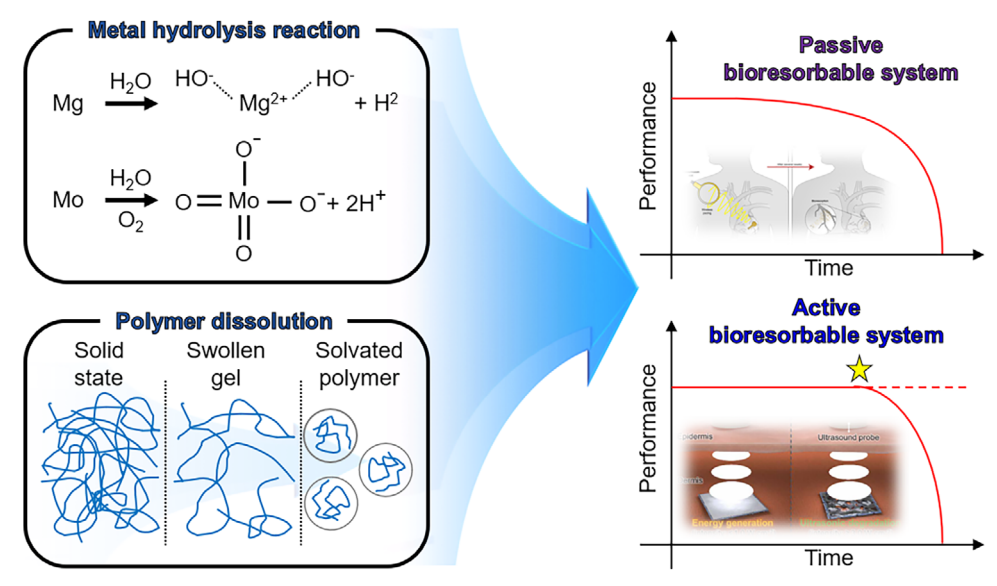


Figure 1. Bioresorbable electronics concept design. Schematic illustration of the hydrolysis reaction and dissolution processes of bioresorbable metals and polymers. Devices based on these materials, controlled by various factors, rapidly lose performance after achieving their intended purpose.

Power sources of bioresorbable systems are another requisite factor determining suitabilty for telemedicine or hospital use (Figure 2).[27] The electromagnetic wireless power transfer (WPT) system consists of a high-frequency alternative current (AC) power source, a transmitter coil, a receiver coil tuned to a specific resonance frequency, and an AC-direct current (DC) converter if necessary (Figure 2a). The efficiency is affected by the turns of coils, the distance between coils, the incident angle, etc. Several radio-frequency (RF) bands (e.g., the industrial, scientific, and medical bands of 13.56, 27.12, 915, and 2450 MHz) are potential candidates. Among the frequencies, a specific frequency of 13.56 MHz enables high-efficiency power transmission and reception for implantable medical systems and supports near-field communication (NFC) with satisfying ISO/IEC 15693 recommendations. [28] Another candidate is the piezoelectric nanogenerator that converts mechanical strain to electricity (Figure 2b). Piezoelectric constant, strain changes, and material permittivity determine output AC power.^[29,30] Recently, various biodegradable materials such as amino acid-based peptides, cellulose derivatives, and silk fibroin have been explored as promising alternatives for piezoelectric nanogenerators due to their biocompatibility and degradability in physiological environments.[31,32] The thin-layered piezoelectric structure also utilizes implantable mechanical sensors.[33] The other candidate is the triboelectric nanogenerator (TENG) that generates electricity by triboelectrification and electrostatic induction (Figure 2c). [34] Output power performance is affected by surface charge density, the dielectric constant, and the gap distance between the top and bottom electrodes. Secondary batteries that store specific power for long-term usage are promising energy storage systems to overcome the limitations of energy transfer and nanogenerators such as limited power transfer conditions and output power (Figure 2d).[35] Chemical reactions at the anode and cathode discharge continuous DC output and external energy sources such as RF WPT or nanogenerators recharge the battery to prolong its lifespan.[36]

This review summarizes bioresorbable materials from polymers to metals, and the recent developments in bioresorbable electronic applications and energy sources. The content begins with an overview of bioresorbable polymers, their chemical composition and hydrolysis process. A subsequent section focuses on chemical reactions of bioresorbable metals. Application examples highlight recent progress ranging from skin-interfaced systems to implanted sensors, describing the structure, performance, and bioresorbable properties (Figure 3). Current bioresorbable skin-interfaced systems face key challenges in achieving optimal flexibility and piezoelectric performance, which drives ongoing research efforts. Emerging design strategies overcome the rigidity and mechanical instability of bioresorbable triboelectric materials by applying glycerol as a plasticizer.[37-39] For bioresorbable stimulators and sensors, piezoelectricity enhancement strategies focus on introducing new materials (i.e., PVA,[2] glycine[12]) during fabrication or implementing microdome structures.[11] Implantable bioresorbable applications utilize structural enhancements and optical sensing approaches to overcome limitations in sensor sensitivity, and adopt laser-based fabrication techniques to achieve highresolution Electrocorticography (ECoG). [40] A concluding section summarizes the current advances and discusses opportunities for future research.

2. Hydrolysis Properties of Bioresorbable Polymers

Bioresorbable polymers such as PVA, PLA, PGA, polycaprolactone (PCL), polyanhydride (PA), poly(1,8-octanediol-co-citrate) (POC), polybutylene succinate (PBS), poly(carboxybetaine) degradable urethane (PCBDU), poly(3-hydroxybutyrate-co-3-hydroxyvalerate) (PHBV), polyethylene glycol diacrylate (PEGDA), poly(glycerol-co-sebacate) (PGS), poly-L-lactic acid (PLLA), poly-D,L-lactic acid, poly(lactic-co-glycolic acid) (PLGA), poly(1,8-octamethylene-citrate-co-octanol) (POCO), etc., have well-established dissolution processes and roles as scaffolds,

onlinelibrary.wiley.com/doi/10.1002/aelm.202400997 by Chung-Ang University, Seoul, Wiley Online Library on [06/07/2025]. See the Terms.

nelibrary.wiley.com/terms-and-conditions) on Wiley Online Library for rules of use; OA articles are governed by the applicable Creative Commons

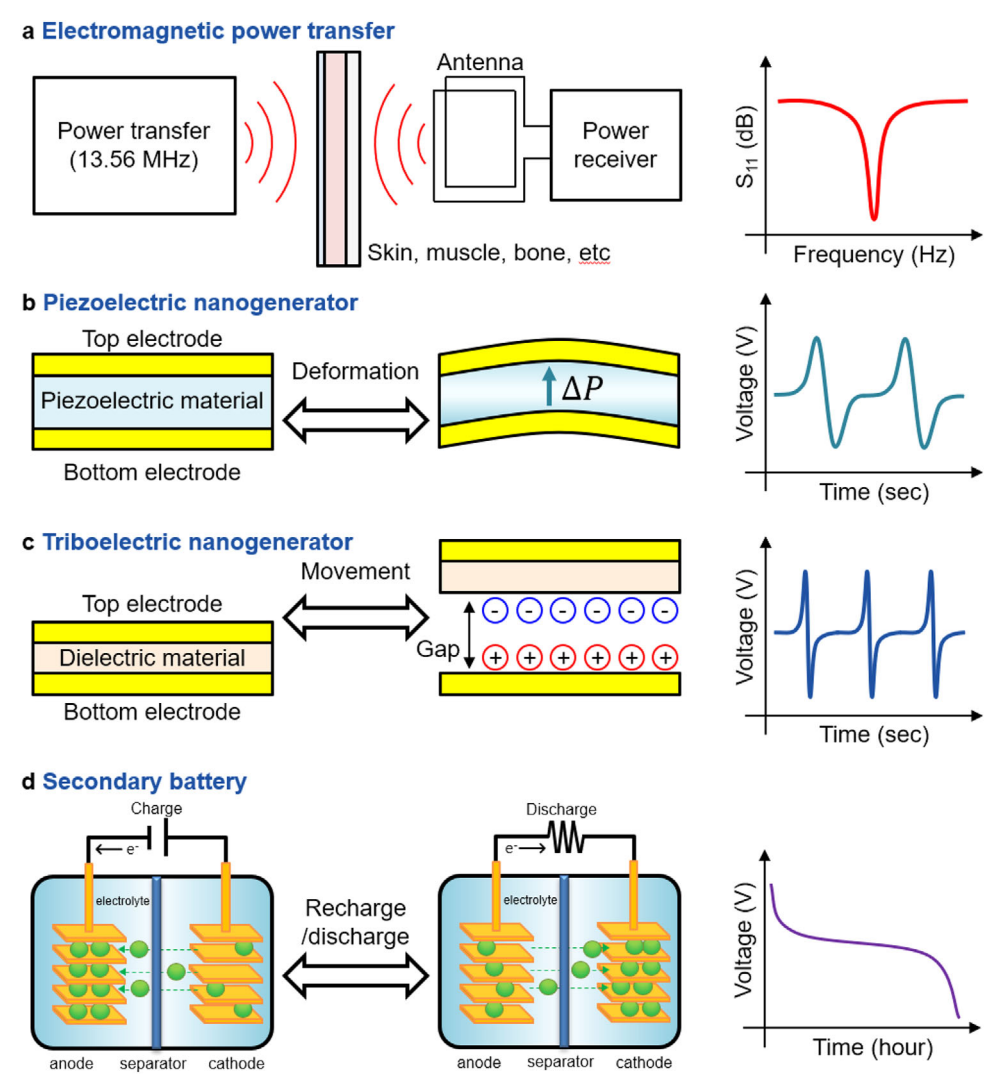


Figure 2. Powering systems of bioresorbable systems. Schematic illustration of the configuration and power of a) electromagnetic power transfer, b) piezoelectric nanogenerator, c) TENG, and d) secondary battery.

drug eluting polymers, matrices, and adhesives in bioresorbable applications (**Figure 4**).^[46] Surface area to volume ratio, pH, temperature, and the existence of enzymes affect the dissolution rate of bioresorbable polymers (**Table 1**).

PVA, a copolymer of vinyl alcohol and vinyl acetate, has abundant hydroxyl groups, which readily absorb water. Hydrogen bonds in the water molecules interact with these hydroxyl groups, dissolving PVA in water. PLA from renewable resources such as corn flour undergoes hydrolytic processes in biofluid and decomposes to CO₂ and H₂O. PGA is a semicrystalline polymer that has amorphous regions and highly organized crystalline regions. The water penetration into amorphous regions causes the disintegration of the tie-chain segments into small fragments; imperfect areas such as vacancies, defects, and boundaries in highly crystalline regions have slower hydrolysis degradation than that of the amorphous regions. Shortchain fragments convert into monomeric acids and are subsequently metabolized. Thermoplastic PCL is another example of a semicrystalline polymer, which has a slow degradation rate. [50]

Amorphous regions of PCL are mainly decomposed by enzymes not usually found in animal and human bodies, but hydrolytic degradation can take a long time. The hydrolytic breakdown of the polymer backbone and hydrolytic chain scission produce monomers and acid by-products. PA controls the hydrolysis rate by varying the ratio of hydrophobic or hydrophilic monomers.^[51] The surface degrades into homopolymers such as poly sebacic acid with a linear degradation and the core crystalline region gradually affects over time and depolymerizes into water-soluble fragments and monomers. POC, copolymer of citric acid (CA) and 1-8-octanediol (OD), is a hydrophilic polymer with good water absorbability.^[52] Since the degradation rate of CA is faster than that of OD, the cross-linking network of POC is gradually lost, leading to a collapse of POC. PBS is one of the aliphatic polyesters with high hydrolyzability in water, which decomposes to succinic acid, and butane-1,4-diol (BD).[53] The measurement of the total organic carbon of the surrounding water after hydrolytic degradation confirms BD tends to form volatile compounds such as ethylene glycol. An elastic bioresorbable polymer

2199160x, 2025, 10, Downloaded from https://adv

onlinelibrary.wiley.com/doi/10.1002/aelm.202400997 by Chung-Ang University, Seoul, Wiley Online Library on [06/07/2025]. See the Terms

and-conditions) on Wiley Online Library for rules of use; OA articles are governed by the applicable Creative Commons

www.advancedsciencenews.com

www.advelectronicmat.de

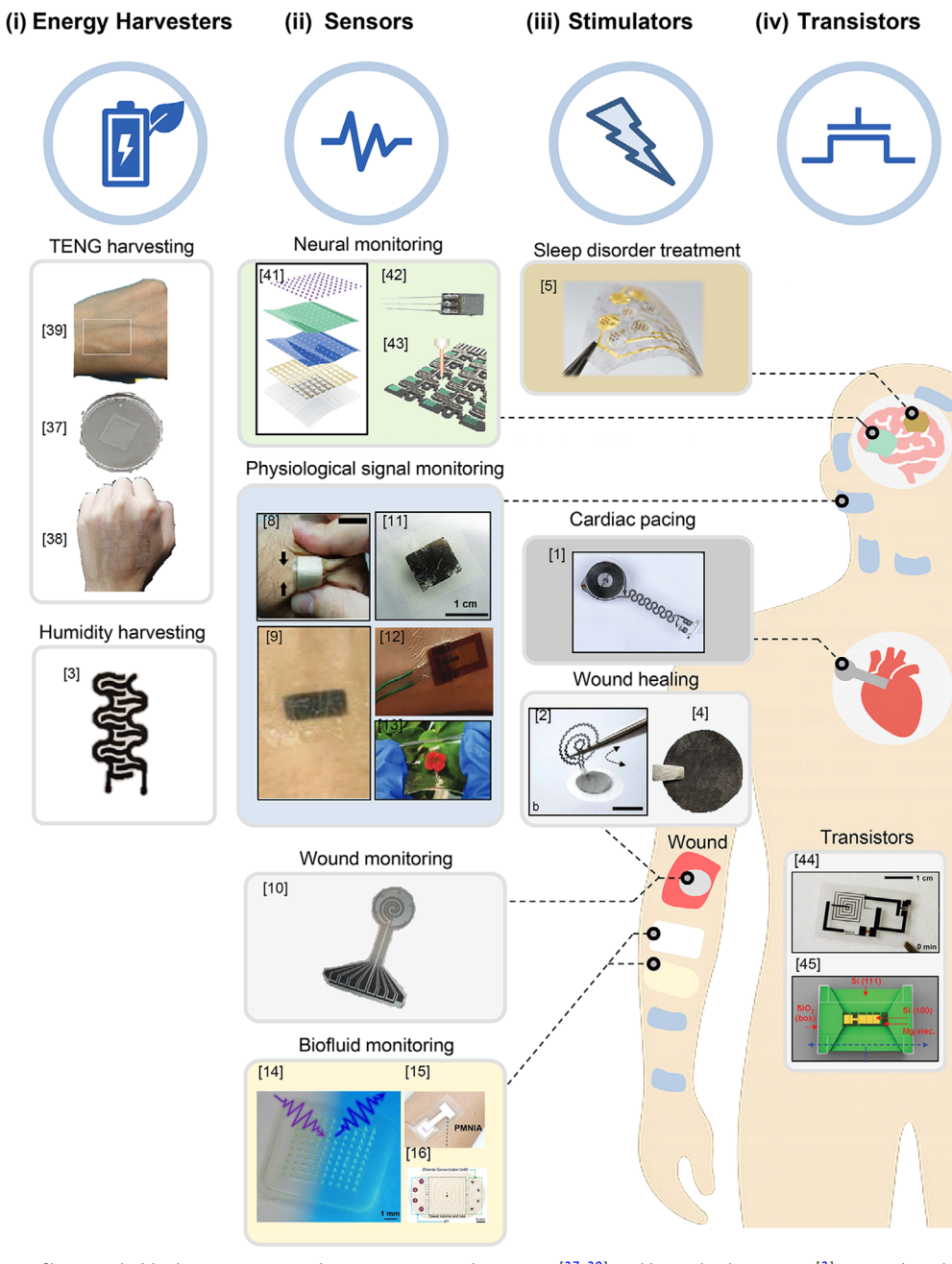


Figure 3. A summary of bioresorbable devices. i) Energy harvesters: TENG harvesting^[37–39] and humidity harvesting^[3]. Reproduced with permission.^[39] Copyright 2022, Wiley-VCH GmbH. Reproduced with permission. [37] Copyright 2023, Elsevier B.V. Reproduced with permission. [38] Copyright 2020, Elsevier B.V. Reproduced with permission. sevier B.V. Reproduced with permission.^[3] Copyright 2020, National Academy of Sciences. ii) Sensors: neural monitoring,^[41–43] physiological signal monitoring,^[8, 9, 11–13] wound monitoring,^[10] and biofluid monitoring.^[14–16] Reproduced with permission.^[41] Copyright 2023, Wiley-VCH GmbH. Reproduced with permission. [42] Copyright 2016, Springer Nature Limited. Reproduced with permission. [43] Copyright 2022, Nature Portfolio. Reproduced with permission.^[8] Copyright 2023, Elsevier B.V. Reproduced with permission.^[9] Copyright 2018, Wiley-VCH GmbH & Co. KGaA. Reproduced under the terms of the CC-BY Creative Commons Attribution 4.0 International license.^[11] Copyright 2021, Wiley-VCH. Reproduced with permission.^[12] Copyright 2023, Wiley-VCH GmbH. Reproduced with permission. [13] Copyright 2023, Wiley-VCH GmbH. Reproduced under the terms of the CC-BY Creative Commons Attribution 4.0 International license. [10] Copyright 2024, Wiley-VCH. Reproduced with permission. [14] Copyright 2023, The American Association for the Advancement of Science. Reproduced under the terms of the CC-BY Creative Commons Attribution 4.0 International license. [15] Copyright 2022, Nature Portfolio. Reproduced under the terms of the CC-BY Creative Commons Attribution 4.0 International license. [16] Copyright 2023, Wiley-VCH. iii) Stimulators: sleep disorder treatment, [5] cardiac pacing, [1] and wound healing, [2,4] Reproduced under the terms of the CC-BY Creative Commons Attribution 4.0 International license. [5] Copyright 2024, Nature Portfolio. Reproduced with permission. [1] Copyright 2022, The American Association for the Advancement of Science. Reproduced with permission.^[2] Copyright 2024, The American Association for the Advancement of Science. Reproduced with permission. [4] Copyright 2023, Wiley-VCH GmbH. iv) Transistors. Reproduced with permission. [44] Copyright 2012, The American Association for the Advancement of Science. Reproduced with permission. [45] Copyright 2013, Wiley-VCH GmbH & Co. KGaA.

onlinelibrary.wiley.com/doi/10.1002/aclm.202400997 by Chung-Ang University, Seoul, Wiley Online Library on [06/07/2025]. See the Terms and Conditions (https://onlinelibrary.

inditions) on Wiley Online Library for rules of use; OA articles are governed by the applicable Creative Commons

Figure 4. Bioresorbable polymers. Schematic illustration of the bioresorbable polymers (e.g., PVA, PLA, PGA, PCL, etc.).

of PCBDU is synthesized by copolymerizing hexamethylene diisocyanate, carboxybetaine (CB) diols, and PCL diol.^[54] Regular ester bonds and beta-amino ester bonds undergo hydrolysis in water, resulting in the generation of charged anions and cations from ester bonds of the CB diols and carboxylic acids from the ester bonds in PCL segments. Breakage of the chains and the existence of charged cations and anions accelerate water penetration. PHBV, a copolymer of hydroxybutyrate and hydroxyvalerate, has a high level of cell adhesion without activation of the hemostasis system but exhibits the coagulation system and the complement reaction. Hydroxyvalerate in PHBV contributes to decreased melting temperature, elastic modulus, and tensile strength. Abiotic phenomena such as mechanical stress, oxidation, etc., and hydrolysis mechanisms decompose and mineralize the PHBV. Afterward, enzymatic hydrolysis reduces the polymer chain length into monomers, and assimilates into biomass,

Table 1. Key physicochemical properties of bioresorbable polymers (e.g., PVA, PLA, PGA, PCL, PA POC, PBS, PCBDU, PHBV, PEGDA, PGS, PLLA, PLGA) relevant for electronic device platforms (representative values; may vary depending on molecular weight, crystallinity, and processing conditions).

Polymer	Dissolution rate	Water diffusivity [cm ² s ⁻¹]	Swelling ratio [%]	T _g [°C]	T _d [°C]	Tensile strength [MPa]	Elongation [%]	Refs.
PVA	Days-weeks	$\approx 10^{-6}$ to 10^{-5}	30–80	≈85	≈230	30–70	100–300	[47]
PLA	Weeks-months	$\approx 10^8$	10–20	≈60	≈280	50-70	2–10	[48]
PGA	Days-weeks	$\approx 10^{-7}$	5-10	≈35	≈250	70–100	3–8	[49]
PCL	Months	$\approx 10^{-8}$	4-10	≈-60	≈250	10–16	300-600	[50]
PA	Weeks-months	≈10 ⁻⁷	10–20	≈50	≈250	20–40	100–200	[51]
POC	Days-weeks	$\approx 10^{-7}$	20-40	≈-20	≈200	0.5-1.5	80–120	[52]
PBS	Weeks-months	$\approx 10^{-7}$	5-15	≈-32	≈280	25-45	100–300	[53]
PCBDU	Weeks-months	$\approx 10^{-8}$	5-15	≈10	≈250	30–50	50-100	[54]
PHBV	Weeks	$\approx 10^{-7}$	5-15	≈5	≈260	30-40	10–20	[55, 56]
PEGDA	Hours-days	$\approx 10^{-6}$	40-70	−60 to −40	≈180	0.1-1.0	50-200	[57]
PGS	Days-weeks	≈10 ⁻⁷	20–40	≈-20	≈200	0.5-2.0	100–150	[58]
PLLA	Months	$\approx 10^{-8}$	5-10	≈60	≈280	50-70	5-10	[59]
PLGA	Days-weeks	$\approx 10^{-7}$	10–20	45–55	≈260	40–60	2–10	[60]

ADVANCED SCIENCE NEWS

www.advancedsciencenews.com



www.advelectronicmat.de

H₂O, and CO₂. PEGDA which develops from polyethylene glycol is a commonly utilized hydrogel, which has hydrolyzable esters backbone groups and oxidable ether backbone groups; hydrolysis is a primary dissolution process.[57] The alkaline condition, high molecular weight, and low concentration can accelerate the hydrolysis process. Swelling by biofluid during in vitro experiments also decreases crosslink density and accelerates the hydrolysis process. Polycondensation of glycerol and short-chain sebacic acid forms hydrogen bonds between each hydroxyl group to achieve biocompatible and hydrophilic PGS.^[58] In vitro and in vivo dissolution tests demonstrate different behaviors due to the existence of enzymes and macrophages that cause an accelerated dissolution rate; in vivo test shows five times faster dissolution rate. PLLA is one of the semicrystalline materials having different dissolution behaviors between amorphous and crystal regions.^[59] The amorphous region facilitates elastic behaviors and crystalline regions where high-ordered compact structure contributes to mechanical properties of stiffness, and strength. Ester bonds in amorphous regions initiate hydrolysis, decreasing elasticity, chain length, and molecular weight. Penetrated water molecules through amorphous regions accelerate the degradation rate. PLGA, one of the U.S. Food and Drug Administration (FDA)-approved biodegradable polymers, is usually utilized as an encapsulation layer of drugs. [60] As the proportion of PGA increases and the average molecular weight of PGA and PLA decreases, the bioabsorption rate of PLGA increases. Both hydrolysis and biodegradation processes occur in backbone ester bonds. Water penetration into the PLGA matrix causes uniform bulk degradation. Increasing carboxylic end groups increase autocatalytic hydrolysis degradation. These materials present good biocompatibility but nanoparticles resulting from hydrolysis can have a local and mild tissue reaction.

3. The Chemical Reaction of Bioresorbable Metals

The presence of bioresorbable metals in biomedical applications offers electroconductivity and high stiffness, which extend the application fields from fixtures to electronics. Mg, Zn, Fe, Mo, W, and silicon (Si) are well-known bioresorbable metals (Figure 5).[61] The hydrolysis processes of Mg, Zn, and Fe are $Mg + 2H_2O \rightarrow Mg(OH)_2 + hydrogen gas (H_2), Zn + 2H_2O \rightarrow$ $Zn(OH)_2 + H_2$, and $4Fe + 3O_2 + 10H_2O \rightarrow 4Fe(OH)^{4-} + 4H^+$, respectively, and corresponding cathodic reactions are 2H₂O + 2e⁻ \rightarrow H₂ + 2OH⁻ for Mg and Zn, and 2H₂O + O₂ + 4e⁻ \rightarrow 4OH⁻ for Fe.[55] The hydrolysis processes of Mo, W, and Si are 2Mo + $2H_2O + 3O_2 \rightarrow 2H_2MoO_4$, $2W + 2H_2O + 3O_2 \rightarrow 2H_2WO_4$, and $Si + 4H_2O \rightarrow Si(OH)_4 + 2H_2$, respectively, and have much lower dissolution rates than Mg, Zn, and Fe.[62] Anode and cathode of bioresorbable metals show different dissolution rates due to electrolytic corrosion, in which the anode has much faster dissolution rate than cathode. [63] Metal oxides that can form on the anode during electrostimulation (ES) have different water solubilities. Magnesium oxide (MgO), for example, dissolves in water $(MgO + H_2O \rightarrow Mg(OH)_2)$, and molybdenum trioxide (MoO_3) can dissolve in water $(MoO_3 + H_2O \rightarrow MoO_4^{2-} + 2H^+)$; [64] ZnO is almost insoluble in water, but dissloves in acid (e.g., ZnO + $2HCl \rightarrow ZnCl_2 + H_2O$) and in alkalis (e.g., ZnO + 2NaOH + $H_2O \rightarrow Na_2[Zn(OH)_4]$; iron oxide (Fe₂O₃) and tungsten trioxide (WO₃) show the hydrolysis process of Fe₂O₃ + H₂O \rightarrow Fe(OH)₃

and $WO_3 + H_2O \rightarrow H_2WO_4$, respectively, that have a poor water solubility. Silicon oxide (SiO₂) show the hydrolysis process of $SiO_2 + 2H_2O \rightarrow Si(OH)_4$. Existence of sodium chloride (NaCl) in biofluid or phosphate-buffered saline (PBS) can react with metal oxides (e.g., $ZnO + 2NaCl + H_2O \rightarrow ZnCl_2 + 2NaOH$, $Fe_2O_3 +$ 6NaCl + 3H₂O \rightarrow 2FeCl₃ + 6NaOH, and WO₃ + NaCl + H₂O \rightarrow NaHWO₄ + HCl), whose products are highly water soluble.^[65] Additionally, chloride ions in solution initiate breakdown of the metal(OH), layer on metal surface. Some bioresorbable metals make acidic products as a result of dissolution. In addition to metals, silicon-based materials particularly in nanostructured forms such as nanowires, nanoribbons, and nanomembranes demonstrate bioresorbability through hydrolysis in aqueous environments. This process occurs via a chemical reaction with water (Si $+4H_2O \rightarrow Si(OH)_4 + 2H_2$), producing orthosilicic acid (Si(OH)₄) and H₂.

4. Bioresorbable Skin-Interfaced Applications

Skin-interfaced systems enable continuous, noninvasive monitoring of physiological signals through direct skin contact, maintaining conformal adhesion through mechanical flexibility and stability. Conventional platforms utilize flexible elastomers such as polydimethylsiloxane (PDMS), polyimide (PI), polyethylene terephthalate (PET), and Ecoflex. Their non-bioresorbable nature requires manual removal and contributes to e-waste accumulation. In contrast, bioresorbable platforms dissolve under physiological or environmental conditions, leaving biocompatible byproducts from their integrated dissolvable metals, polymers, and auxiliaries. This section explores recent developments in bioresorbable skin-interfaced systems, focusing on material selection and dissolution characteristics. The subsequent section presents a functional classification of these systems into three categories: stimulation, [1-6] energy harvesting, [3, 37-39] and sensing.[7-16]

4.1. Stimulation Systems

Stimulators are devices designed to induce physical or chemical effects for therapeutic purposes. Physical stimulators typically deliver electrical pulses for heart rhythm regulation^[1] and wound healing,^[2] or thermal actuation for biomedical treatment.^[3] Chemical stimulators deliver therapeutic agents such as metal ions (Cu²⁺),^[4] hormones (melatonin),^[5] or nucleic acids (VEGF-165 plasmid DNA)^[6] for wound healing, sleep disorder treatment, and neovascularization, respectively. Bioresorbable stimulators offer significant advantages by reducing surgical complications and enabling versatile drug administration. These devices temporarily interface with target sites before completely dissolving, reducing inflammation risks and complications for device removal. Table 2 summarizes bioresorbable stimulation systems in terms of their target applications, stimulation mechanisms, operating parameters, and constituent bioresorbable materials and components.

4.1.1. Physical Stimulation Systems

Recent advancements in electrical stimulation technology include the development of a wireless pacemaker with only the



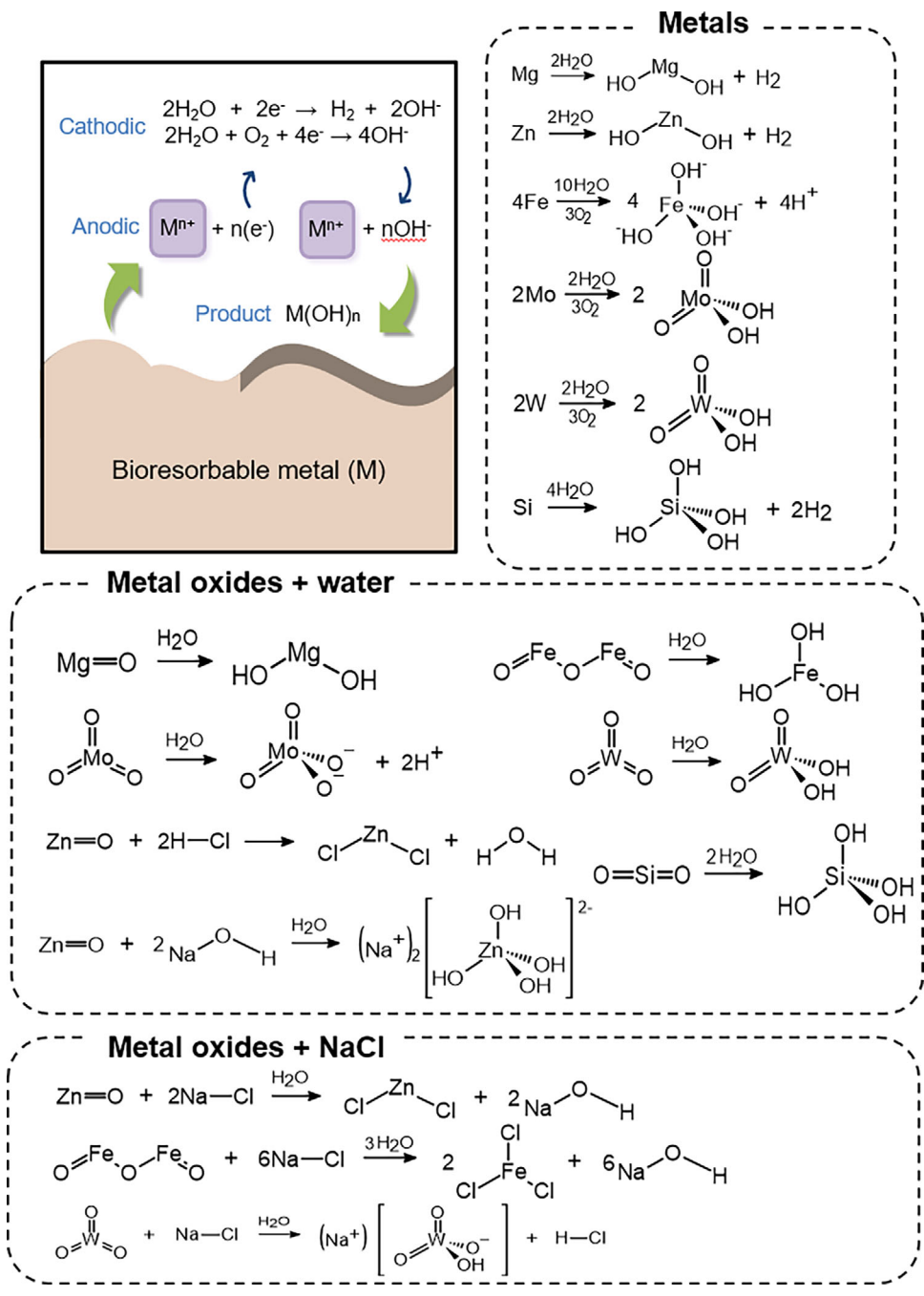


Figure 5. Bioresorbable metals. Schematic illustration of the chemical reactions involved in the hydrolysis reaction of bioresorbable metals and metal oxides with water and NaCl.

implantable parts made to be bioresorbable.^[1] This device operates as a closed-loop system comprising three key components: skin-interfaced sensing modules, a hand-held control module, and a bioresorbable, wireless, implantable electrical stimulator (**Figure 6a**). The cardiac, hemodynamic, and respiration sensing modules support comprehensive physiological monitoring. The control module (e.g., smartphones) receives raw data from these sensing modules, extracting electrocardiogram (ECG), photoplethysmogram, heart rate (HR), and respiratory rate data.

Based on this information, it sends pacing commands to the skininterfaced cardiac module, which then controls the implanted stimulator using a transmitter coil. The bioresorbable stimulator incorporates an RF power harvester and two stimulation electrodes. A circular receiver (RX) coil and a Si nanomembrane (NM) diode comprise the harvester, subcutaneously placed to maximize the WPT efficiency. Stretchable, serpentine interconnects link the harvester to myocardium-contacting electrodes, facilitating targeted DC electrical stimulation. Thin films



www.advelectronicmat.de

Table 2. Summary of bioresorbable stimulation systems.

Туре	Target application	Stimulation mechanism	Stimulation parameters	Bioresorbable materials	Bioresorbable parts
Physical	Cardiac pacing[1]	Monophasic electrical	Power	b-DCPU	Stimulator encapsulation
		pulse	4.5 mW	Мо	RF power harvester (coil) Interconnect Electrodes
	Wound healing ^[2]	Voltage pulse	V_{oc}	γ -glycine PVA	Piezoelectric biofilm
			220 mV Electric field 220 mV mm ⁻¹	PLA	Encapsulation
				Мо	Electrodes
			220 mV mm ⁻¹	Si	PIN diodes
	Biomedical treatment ^[3]	Heat	Heating temperature 125 °C	Water-soluble paper	Entire thermal stimulator
Chemical	Wound healing ^[4]	Cu ₂₊ ion delivery	100 μg cumulative release in 6 days (PBS solution with pH 5.0)	e-ADM	Entire electronic skin
	Sleep disorder treatment ^[5]	Melatonin delivery	25 wt% Melatonin-loaded MN	PLGA	Microneedles (MNs)
	$Neovas cularization ^{[6]} \\$	VEGF-165 plasmid DNA delivery	pVEGF165 100 μg	Porous silicons	Nanoneedles (NNs)

of Mo (10- μ m-thick) constitute the primary bioresorbable components, including the harvester, interconnects, and electrodes. Bioresorbable dynamic covalent polyurethane (b-DCPU) (100- μ m-thick) encapsulates the stimulator, excluding the contact site of the electrodes. The electrode contact sites incorporate a PLGA steroid-eluting patch (4.64 \times 3.34 mm²) to mitigate inflammation or fibrosis during cardiac pacing.

In vivo studies with canine whole-heart models (adult hound dogs, 27-36 kg) demonstrate WPT and cardiac pacing. The stimulating device delivers a monophasic output (4.5 mW power, 3 Hz frequency, 6.6 ms pulse width) when the cardiac module generates a pulsed 6 V_{DD} AC signal. This induced a ventricularly paced rhythm (180 bpm) from the intrinsic sinus rhythm (150 bpm). Ex vivo studies with a Langendorff-perfused human whole-heart model demonstrate the closed-loop autonomous treatment capability, stimulating temporary bradycardia with an HR below a predetermined threshold (54 bpm). The bioresorbable stimulator maintained functionality for up to 32 days in PBS (pH 7.4, 37 °C) and in an in vivo rat model, due to the slow degradation rate of Mo (≈20 nm day⁻¹).^[62] This degradation period exceeds the therapeutic window of conventional temporary pacemakers (7 days), demonstrating its long-term pacing and biocompatibility. Adjusting the device thickness, component materials, and applied external stimuli allows for tuning the lifetime to satisfy the needs of patients and treatment period. [26,66,67] The device completely degrades and disappears within 500 days, eliminating removal complications.

Another advancement is the bioresorbable wireless piezoultrasound electrotherapy device (b-WPUE) for wound healing. [2] This skin-interfaced device converts external ultrasound (US) waves to electrical stimulation, which is applied to the wound site, then biodegrades after recovery. The b-WPUE features a power harvester for acoustic-to-electric conversion, and two electrodes for stimulation (Figure 6b). The harvester includes Mo-deposited γ-glycine/PVA film and two Si positive-intrinsic-negative (PIN) diodes. The piezoelectric biofilm (10-mm diameter) generates AC electricity under US vibration, which the diodes rectify to DC output. Applying 1-MHz US treatment to a mixture of glycine and PVA solution accelerates crystallization and inhibits agglomeration, yielding pure γ -glycine crystals oriented for enhanced piezoelectric effect. The Mo electrodes (50-µm-thick) feature a circular design with three concentric rings, composed of serpentine flower-like patterns. Here, one electrode comprises the central circle combined with the outermost ring, while the other is the middle ring. Each ring has a width of 0.5 mm, spaced 1 mm apart from its neighbors. This unique design enhances electrotherapeutic effectiveness by providing efficient stimulation across the wound area. The PLA films (50-µm-thick) encapsulate the harvester and the electrode structures, leaving only the contact areas of the electrodes exposed. A PVA gel secures the harvester and electrodes in their folded configuration.

Benchtop studies, computational predictions, and in vivo experiments validate the performance of b-WPUE. For benchtop studies, a lead zirconate titanate (PZT) ceramic disk (diameter: 25 mm) emits US waves (center frequency of 1 MHz) into a tank filled with deionized (DI) water (transmission medium). At a trigger signal of 110 V_{PP}, the b-WPUE generates a rectified open-circuit output voltage (V_{oc}) of \approx 220 mV, resulting in an electric field of 220 mV mm⁻¹ across 1-mm-spaced electrodes. This field strength aligns with the finite element analysis results, surpassing the 100 mV mm⁻¹ threshold known to accelerate wound healing.[68-70] In vivo evaluations involved rodent models with artificial wounds (6 mm diameter), divided into four groups: control (no treatment), US stimulation only, b-WPUE without US stimulation, and b-WPUE with US stimulation. The US-stimulated groups received US waves (0.1 W cm⁻², 60% duty cycle) from the plate transducer for 5 min daily over 7 days. Wound healing progress was ≈40% faster in the b-WPUE with

2199160x, 2025, 10, Downle

Hibrary.wiley.com/doi/10.1002/aelm.202400997 by Chung-Ang University, Seoul, Wiley Online Library on [06/07/2025]. See the Terms and Conditions

onditions) on Wiley Online Library for rules of use; OA articles are governed by the applicable Creative Common

Figure 6. Stimulation systems. Bioresorbable materials are marked in blue. a) Photographs of skin-interfaced sensing modules, a bioresorbable electrical stimulator along with bioresorption process and stimulation output power. Reproduced with permission. [1] Copyright 2022, The American Association for the Advancement of Science. b) Schematic illustration of b-WPUE, photographs of bioresorption process, and Voc under various trigger voltages. Reproduced with permission. [2] Copyright 2024, The American Association for the Advancement of Science. c) Image of e-ADM. Reproduced with permission. [4] Copyright 2023, Wiley-VCH GmbH. d) Schematic illustration of SOP, images of spatiotemporal activation of SOP with 7 MN patches (top right, activating from i to iv), PLGA MN, Mel-MN, Au-Mel-MN (bottom center), and bioresorbed MN after 24 h (bottom right). Reproduced under the terms of the CC-BY Creative Commons Attribution 4.0 International license. [5] Copyright 2024, Nature Portfolio.

US group compared to others. Here, the b-WPUE with US group achieved complete recovery in \approx 10 days, while other groups required 15 days for comparable healing.

NFC module

In vitro and in vivo studies confirmed the device's bioresorbability. In a 1× PBS (pH 7.4, 37 °C), the PLA-encapsulated γ -

glycine/PVA biofilm degraded within 2 weeks, with complete degradation of the b-WPUE residue (mainly electrodes) occurring within 36 weeks. The output voltage of b-WPUE decreased by 10% at day 6, declined sharply at day 12, and became nearly undetectable by day 14. When implanted in the backs of mice, the

1_mm

1X DPBS @

65 °C

1_{mm}

Au-Mel-MN





www.advelectronicmat.de

biofilm gradually degraded from days 1 to 10. This degradation timeline aligns with the complete wound recovery time observed in the b-WPUE with US group, demonstrating an appropriate match between the healing process and the device's bioresorption rate. Adjusting the thickness of the encapsulation layers and electrodes allows for programming the functional lifetime of the device. The b-WPUE devices leave only harmless by-products and eliminate complications related to device extraction.

An additional approach is the bioresorbable pencil-drawn thermal stimulator for wound healing.^[3] This device promotes wound healing through Joule heating of pencil-drawn conductive traces. The design incorporates serpentine conductive traces on kirigami-cut office copy paper (100-µm-thick). This serpentine structure demonstrates robustness to mechanical deformations, exhibiting a 20% resistance change at a 1.5 mm bending radius. Kirigami cuts enhance the stretchability of the paper substrate.^[71] The pencil-drawn serpentine graphite traces on kirigami-cut papers maintain stable resistance up to 150% tensile strain, with 8% resistance change after 1000 bending cycles (6-mm bending radius) and 0.1% resistance change after uniaxial stretching tests (100% tensile strain). Repeated ruler-guided drawing of a 9B sketch pencil for 1–15 cycles produces conductive traces with sheet resistance ranging from 10 k Ω sq⁻¹ to 160 Ω sq⁻¹, while this study employed 15 cycles for 6-µm-thick traces. A biocompatible Silbione coating further improves the office-copy paper's contact quality while maintaining breathability, a desirable feature for on-skin electronics that accelerates skin perspiration evaporation, minimizes sweat accumulation, and mitigates inflammatory reactions.[72-74] When spray-coated with an optimal Silbione-to-paper weight ratio of 5:100, the adhesion force increases from 0.01 to 0.85 N while exhibiting 2137 g m⁻² day⁻¹ water vapor transmission rate (WVTR), significantly higher than human skin (204 g m⁻² day⁻¹). [75] Alternatively, simply replacing the office-copy paper with a commercial adhesive paper enhances the contact quality, eliminating the need for complex coating processes.

On-skin thermal stimulator provides one example of the versatility of presented on-skin electronics. The device provides high electrical conductivity and rapid thermal stimulation, reaching 125 °C within 30 s when applied with 40 V. Its serpentine structure ensures adaptability to various body movements. By replacing office-copy paper with water-soluble paper, the thermal stimulator becomes bioresorbable. Upon contact with water, the paper quickly degrades, causing the conductive graphite traces to disassemble. This degradation mechanism eliminates the need for device removal and facilitates the transfer of the conductive pattern onto curved human body surfaces through the dissolution process.

4.1.2. Chemical Stimulation Systems

Bioresorbable electronic platforms enable diverse approaches to chemical stimulation. Among these, bioresorbable bioelectronic skin—comprising flexible, epidermally adherent electronic interfaces—serves dual functions by delivering therapeutic agents while providing structural support for healing processes, thereby eliminating the requirement for subsequent explantation procedures.^[4] An acellular dermal matrix (ADM) is a decellular-

ized allograft tissue utilized in medical procedures to promote wound repair processes.^[4,76–78] Once applied to a wound, the ADM serves as a scaffold that supports new tissue regeneration during healing and integrates into the host tissue, eliminating the need for post-treatment removal.^[76–79]

Recently, the integration of carbon nanotubes (CNTs) and copper oxide microspheres with ADM has led to the development of bioresorbable ADM-based electronic skin (e-ADM) that enables motion monitoring and enhances wound healing (Figure 6c).[4] The strain-dependent conductivity of CNTs enables motion monitoring, while copper oxide microspheres provide dual functionality in sterilization and wound repair through their nanoconestructured surfaces (200-nm height) and pH-dependent ion release. The rough surfaces destroy bacterial cell walls through applied shear force. [80,81] In acidic wound environments (pH 5–6), the microspheres release copper ions for sterilization, whereas under physiological conditions (pH 7.4), they maintain low copper ion concentrations to promote cell proliferation and vascularization.[82-84] An in vivo study comparing five groups of specific pathogen-free rats evaluated the wound healing performance: control (no treatment), ADM only, e-ADM only, ADM with ES, and e-ADM with ES. ES groups received two daily 1 h treatments (100 mV mm⁻¹, 25 Hz) separated by a 1 h interval for 7 days. By day 15, the e-ADM groups showed superior wound healing, with wound area reduced to 32.7% (e-ADM only) and 19.3% (e-ADM with ES) compared to 52% (ADM only) and 44% (ADM with ES). The e-ADM exhibited slower biodegradation (10% weight loss) compared to ADM (37%) in collagenase type I/PBS solution (1 U mL⁻¹, 3 mL mg⁻¹ sample, 37 °C) by day 7, attributed to cross-linking between ADM fibers, CNTs, and copper oxide microspheres.

Transdermal drug delivery systems using bioresorbable MN and nanoneedle (NN) structures enable localized, painless drug release upon contact with target tissues.^[5,6] Their controlled degradation allows selective biochemical responses and safe, minimally invasive administration and disposal without trained personnel. Bioresorbable MNs allow controllable release schedules and environment responsiveness through tailored degradation kinetics. A notable MN application is an electrically controlled spatiotemporal on-demand patch (SOP) developed for sleep disorder treatment.^[5] The patch enhances sleep through programmable release of melatonin loaded onto gold-coated bioresorbable MNs. The SOP consists of three main components as illustrated in Figure 6d: a NFC module, melatonin-loaded MN patches, and gold interconnect traces. Each MN patch features an array of MNs coated with 150-nm-thick gold, with one designated patch serving as the counter electrode. Laser-ablated gold interconnects, encapsulated by a PDMS layer (10-µm-thick), establish electrical connectivity between the MN patches and NFC module. The NFC module incorporates an NFC System-on-a-Chip (SoC), an energy harvester, and loaded switches. The energy harvester converts wireless power into 2.5-V DC, which is selectively delivered to MN patches via general purpose input/output-controlled load switches. Upon activation, the voltage induces gold corrosion on the MNs, exposing them to the bioenvironment and triggering melatonin release within 30 s. The MNs subsequently degrade into lactic and glycolic acids.[85]

Benchtop studies confirmed the spatiotemporal release capability using a single SOP with seven MN patches. Each MN





www.advelectronicmat.de

patch included an array of seven MNs (each 1.2-mm height, 0.25-mm diameter, and 1-mm interneedle spacing), loaded with Rhodamine B. In 65 °C 1× Dulbecco's phosphate-buffered saline (DPBS, Corning), sequential Rhodamine B release was achieved by selectively activating individual patches at 30 min intervals (t = 30, 60, 90, and 120 min.), resulting in successful payload delivery from four MN patches over 150 min. Ultraviolet–visible (UV–vis) spectroscopy measurements revealed a stepwise increase in Rhodamine B concentration, with each step corresponding to the 30 min intervals of patch activation. The optical image shown in Figure 6d confirmed the degradation of the activated MN patches.

In vivo experiments evaluated sleep enhancement through two types of MNs (3-mm height and 0.35-0.5-mm diameter): melatonin-loaded MNs (Mel-MNs) and gold-coated, melatoninloaded MNs (Au-Mel-MNs). Stereotaxic implantation placed a single MN in the medial prefrontal cortex of each mouse. The initial experiment included a Mel-MN group and an unloaded MN control group. After one week, the Mel-MN group showed a 42.0% increase in nonrapid eye movement (NREM) sleep duration and a 27.9% decrease in wakefulness over a 3-h monitoring period compared to the control group, confirming melatonin release and its sleep-enhancing effects. The subsequent experiment compared an Au-Mel-MN group against an unloaded and uncoated MN control group. Over 6 h of monitoring, the Au-Mel-MN group showed a 36.7% increase in NREM sleep duration, a 57.8% increase in rapid eye movement sleep duration, and a 26.0% decrease in wakefulness compared to the control group. Electroencephalogram (EEG) delta power density during NREM sleep showed a statistically significant difference in the Au-Mel-MN group (P < 0.01) but not in the Mel-MN group compared to their respective control groups, indicating that Au-Mel-MN induced deeper sleep than Mel-MN. The gold coating slowed MN degradation, which delayed melatonin release and improved sleep-inducing effects by aligning the release timing with the start of the monitoring period, one week after implantation. Uncoated and unloaded PLGA MNs (3-mm height) completely degraded within 24 h during degradation tests in 1× DPBS solution at 65 °C.

NNs enable enhanced intracellular delivery while minimizing cellular disruption compared to MNs. $^{[86]}$ A notable example is the development of a bioresorbable, nucleic acid-loaded NN array for wound healing. $^{[6]}$ The array comprises an 8 \times 8 mm² patch of NNs (600-nm base diameter, 50-nm apical width, 5-µm height) arranged with a 2-µm pitch. Composed of bioresorbable porous silicon, $^{[87]}$ these NNs release their payload during degradation upon skin attachment. Further intracellular nucleic acid delivery is facilitated either by cellular activity or by external physical forces. The porosity of NNs can be tuned between 45% and 70% to control their degradation time, payload volume, and mechanical properties.

In vitro studies validate the NN-mediated gene regulation by injecting Cy-3-labeled small interfering RNA (siRNA) and green fluorescent protein (GFP)-expressing DNA plasmids into HeLa cells. Cell assessment at 48 h post-transfection demonstrated efficiency exceeding 90%, confirmed by GFP expression and siRNA fluorescence. In vivo studies compared three groups of mice models receiving back muscle injections: one injected with 100 µg of human VEGF165 plasmid DNA (pVEGF165) via direct injection, another injected with pVEGF165 using NNs, and a con-

trol group treated with sham surgery without injection. Only NN-mediated delivery resulted in a sixfold increase in blood perfusion and the number of vasculature nodes, with newly formed vessels showing expected immaturity characteristic of pVEGF165 expression. In vitro bioresorption tests in a cell-culture medium at 37 $^{\circ}\text{C}$ revealed progressive degradation of NNs, with complete degradation within 72 h.

Bioresorbable stimulation systems require careful evaluation of their degradation profiles relative to therapeutic needs, but currently lack adaptability to specific therapeutic needs. The Mobased pacemaker^[1] functions for >32 days but requires 500 days for complete resorption, while silicon NNs^[5] degrade rapidly within 72 h. Without sufficient clinical evidence establishing optimal degradation timeframes for different applications, these fixed degradation rates represent a significant limitation. Although the b-WPUE system^[2] shows promising temporal alignment with wound healing processes, and pencil-paper and SOP systems^[3,5] offer some control over degradation initiation, most current technologies cannot dynamically adjust their degradation timing once implanted. Future developments should focus on creating systems with tunable degradation profiles that can be tailored to diverse clinical requirements.

4.2. Energy Harvesting Systems

Energy harvesting technologies address the limitations of conventional battery-powered devices by converting ambient physical and chemical energy into electrical power for devices. Physical energy harvesters employ single-electrode mode TENGs that combine energy harvesting with mechanical signal detection for self-powered tactile sensing.[37-39] Their fundamental structure comprises an electrode layer encapsulated by triboelectric materials, which generate electrical charge through contact electrification and electrostatic induction during contact-separation cycles between the triboelectric layers and external materials (e.g., skin). Chemical energy harvesters complement this approach by converting ionic potential gradients into electrical energy.[3] Electromagnetic power transfer, piezoelectric nanogenerators, and secondary batteries are also gaining attention as useful energy harvesting approaches for in vivo applications. These technologies overcome constraints in operational lifetime, size, and environmental sustainability while meeting growing power demands for diverse Internet of Things (IoT) applications, noninvasive healthcare monitoring, and human-machine interfaces (HMIs). Notably, bioresorbable variants of both harvesting mechanisms prevent e-waste accumulation through their transient properties.[3, 37-39]

4.2.1. Physical Energy Harvesters

Conventional physical energy harvesters utilize synthetic polymers with strong triboelectric properties, including PET, PDMS, and PI. While natural materials like chitosan (CS), [39] sodium alginate (SA), [37] and regenerated silk fibroin (RSF) offer strong triboelectric properties and bioresorbability, their inherent rigidity limits direct application in skin-interfaced devices. Recent fabrication techniques address this limitation through plasticizers



www.advelectronicmat.de

Table 3. Summary of bioresorbable energy harvesting systems.

Туре	Target application	Harvesting mechanism	Harvesting parameters	Bioresorbable materials	Bioresorbable parts
Physical	Energy harvesting ^[39]	Triboelectricity	$V_{\rm oc}$, $I_{\rm sc}$, $Q_{\rm sc}$ 45 V, 0.27 μ A, 16 nC (8 N, 5 Hz contact with PTFE)	Chitosan (CS)	Triboelectric encapsulation layer
	Energy harvesting, self-powered pressure sensing ^[37]		$V_{\rm oc}$, $I_{\rm sc}$ 22 V, 0.37 μ A (15 N, 4 Hz contact w/ PTFE) Peak power 4 μ W (50 M Ω load)	Sodium alginate (SA)	Triboelectric encapsulation layer
	Energy harvesting, self-powered tactile sensing ^[38]		$V_{\rm oc}$, $I_{\rm sc}$ 13 V, 0.6 μ A (3 Hz contact) Peak power 0.8 mW m ⁻² (600 M Ω , 3 Hz)	Regenerated silk fibroin (RSF)	Triboelectric encapsulation layer
Chemical	Energy harvesting ^[3]	Humidity-induced ion gradient	$V_{\rm oc}$ 480 mV (10 M Ω load, 95% relative humidity) 2.1 V (5 parallel-connected devices) $I_{\rm sc}$ 8 μ A (10 Ω load) 32 μ A (5 parallel-connected devices)	Water-soluble paper	Entire energy harvester

such as glycerol, [37–39] sorbitol, [37] and ethylene glycol, [37] These plasticizers enhance the flexibility of natural triboelectric materials by weakening molecular forces and increasing polymeric chain mobility. [88,89] **Table 3** summarizes the bioresorbable energy harvesting systems.

A bioresorbable CS-based bioelectronic skin enables triboelectric energy harvesting.^[39] The skin (10-µm-thick), shown in Figure 7a, integrates bioresorbable microcracked CS membranes as the triboelectric layers with gold nanofiber (AuNF) as the electrode layer. The CS membranes incorporate 7% v/v glycerol as an optimal plasticizer, achieving 87% elongation at break and a 1.3 MPa Young's modulus similar to human skin (0.14-0.6 MPa). [90] The microcracks (0.032 \pm 0.007 μm width) of CS membranes, emerging during the fabrication processes, significantly enhanced the WVTR (1.91 kg m⁻² day⁻¹), comparable to cotton fabrics (3.18 kg m⁻² day⁻¹), while exceeding other conventional materials including PDMS (0.35 kg m⁻² day⁻¹), polyethylene (0.076 kg m⁻² day⁻¹), and commercial sealing films (0.019 kg m⁻² day⁻¹). The high WVTR facilitates sweat evaporation, enhancing wear comfort while minimizing inflammation. The electrode layer consists of gold-sputtered PVA nanofibers and retains a consistent electrical sheet resistance of 25.8 Ω \mbox{sq}^{-1} under 80% strain, demonstrating strain-insensitive conductance suitable for skin-interfaced applications.

Benchtop studies validated the energy-harvesting and pressure-sensing capabilities of the skin. A mechanical linear motor with polytetrafluoroethylene (PTFE) film applied cyclic contact at 8 N load across 1–5 Hz frequencies. The skin device generated a 45 V $V_{\rm oc}$, a short-circuit charge transfer ($Q_{\rm SC}$) of 16 nC, and gradually increasing short-circuit current ($I_{\rm SC}$) from 0.12 to 0.27 μ A. The $V_{\rm oc}$ remained constant after 15000 cycles of continuous loading, demonstrating the device's durability. Applying different weights to the device reveals a pressure sensitivity of 0.012 kPa $^{-1}$ over a range of 0 to 70 kPa, defined by the ratio of normalized voltage change to applied pressure. The device exhibits a 70 ms response time under 5

N loading and unloading cycles, enabling real-time pressure monitoring.

In vitro studies demonstrated the bioresorbability of both the CS membrane and complete device in various solutions. The CS membrane began to bioresorb within 15 min and completely degraded within 1 h in acetic acid at room temperature and within 30 h in pepsase solution at 37 °C. When exposed to hydrogen peroxide ($\rm H_2O_2$) solution, the CS membrane initiated bioresorption within 1 h and completed degradation within 30 h. The complete device showed slower disintegration due to the AuNFs enhancing its impermeability. Bioresorbable metals could replace AuNFs in future designs to achieve complete device bioresorption.

Recently developed SA-based bioresorbable skin enables physical energy harvesting, pressure sensing, joint and muscle movement monitoring, and game controller operations.[37] The device, shown in Figure 7b, comprises top and bottom SA films encapsulating a conductive, flexible layer of silver nanowires (AgNWs). Here, SA, a flexible, transparent, and bioresorbable polysaccharide copolymer derived from seaweed, serves as a positive tribomaterial through abundant electron-donating hydroxyl groups. However, its low ductility and toughness limit its application in skin-interfaced energy harvesters. Incorporating plasticizers, such as glycerol, helps to overcome these mechanical limitations in SA films by weakening molecular forces and increasing polymeric chain mobility. [88,89] At 40 wt%, glycerol increases film elongation at break from 18% to 48%, suitable for skininterfaced applications. Optimal glycerol concentration (30 wt%) balanced flexibility and mechanical strength, as higher concentrations increased elongation but reduced tensile strength. Additional water molecule retention via glycerol's hydroxyl groups further enhances these mechanical properties. This increased water content further improves AgNW adhesion and conductivity, enhancing energy harvesting capabilities compared to pure SA films. The AgNWs layer maintains stable conductivity under mechanical deformation, showing 0.1% resistance increase at 180°

2199160x, 2025, 10, Downloaded

onlinelibrary.wiley.com/doi/10.1002/aelm.202400997 by Chung-Ang University, Seoul, Wiley Online Library on [06/07/2025]. See the Terms

onditions) on Wiley Online Library for rules of use; OA articles are governed by the applicable Creative Commons

www.advancedsciencenews.com

www.advelectronicmat.de

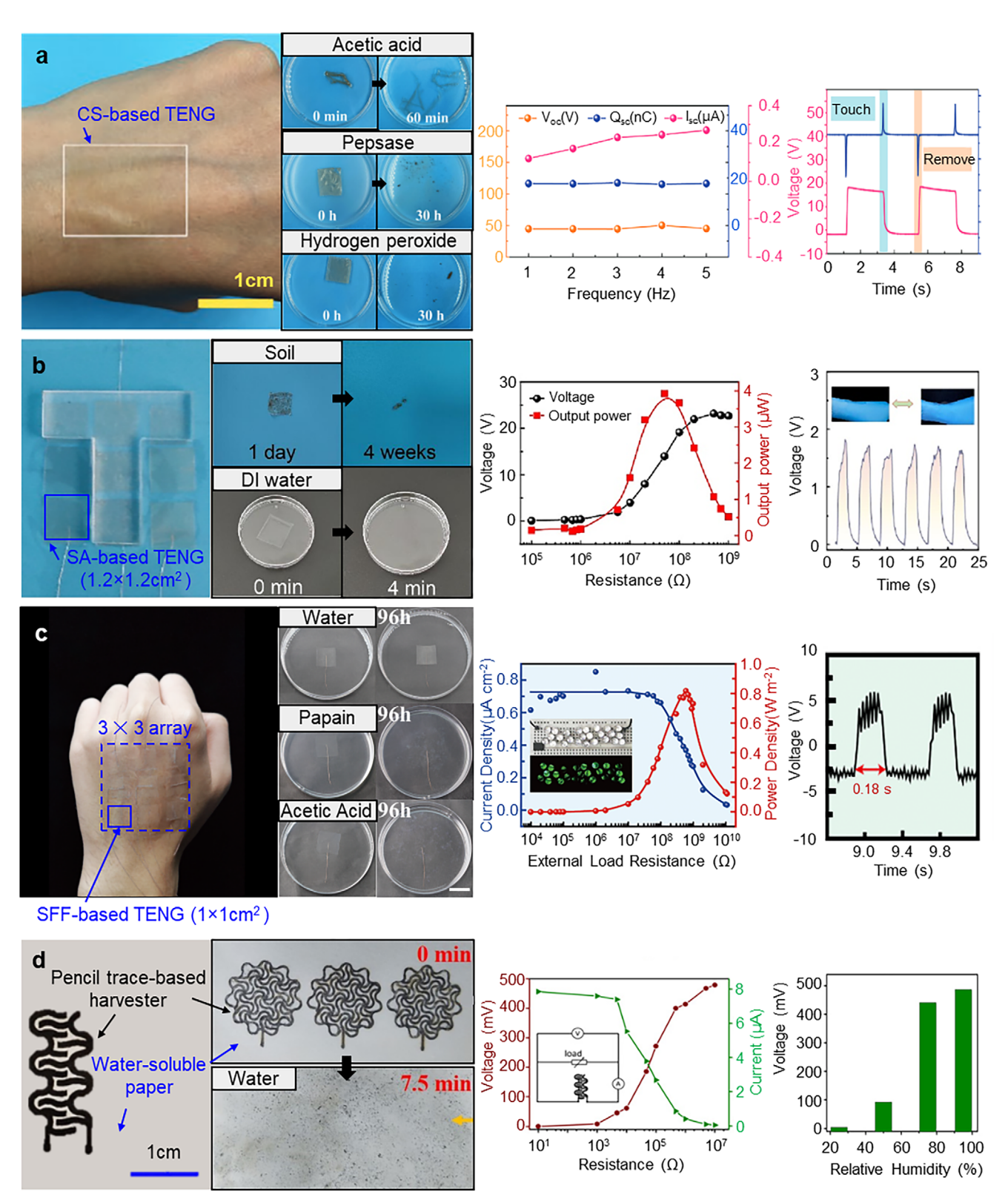


Figure 7. Photographs (left) and key electrical characteristics (right) of energy harvesting systems: a) CS-based bioelectronic skin. Reproduced with permission.^[39] Copyright 2022, Wiley-VCH GmbH. b) SA-based TENG with a T-shaped acrylic plate. Reproduced with permission.^[37] Copyright 2023, Elsevier B.V. c) SFF-based TENG array placed on the skin. Reproduced with permission.^[38] Copyright 2020, Elsevier B.V. d) Pencil trace-based harvester. Reproduced with permission.^[3] Copyright 2020, National Academy of Sciences.

ADVANCED SCIENCE NEWS

www.advancedsciencenews.com



www.advelectronicmat.de

bending and 0.9% increase after 4000 cycles at 150° bending. These results demonstrate advanced durability for flexible skin-interfaced applications.

For energy harvesting, the device generated V_{oc} of 22 V through triboelectric coupling with a PTFE film at the contact interface under cyclic loading (15 N, 0.5-4 Hz) from a linear motor. The I_{SC} increased from 0.22 to 0.37 μA with frequency due to enhanced electron transfer rates.[91] The film dimensions affect V_{oc} and Q_{SC} due to surface charge density effects. Both values decrease with thickness and increase with side length. The device delivered 4 μW peak power at 50 $M\Omega$ optimal load and charged a 1 µF capacitor to 2 V within 120 s at 2 Hz contact frequency. The pressure sensing capability was characterized by dual-regime sensitivities of 0.237 V kPa⁻¹ at <3 kPa and 0.024 V kPa⁻¹ at 3–45 kPa, with a 100 ms response time. For joint/muscle movement monitoring, the device generated distinct voltage signals from various body locations including wrist, finger, forehead, and throat. Furthermore, an HMI system integrated with four skin modules enabled directional game control, translating four skin contacts into four-directional character movement. Benchtop studies confirmed complete dissolution in DI water within 4 min at room temperature and complete degradation in soil within 4 weeks. Additional H₂O₂ exposure test demonstrated SA bioresorbability by destroying the glycosidic bond between β -D-mannuronic acid and α -L-guluronic acid, producing oligomers and reducing solution viscosity by 90% after 4 h.

An RSF-based bioresorbable energy harvester enables touch sensing, pressure detection, and wireless switching for IoT applications. [38] The skin-type device (48.6-µm-thick), shown in Figure 7c, employs silk fibroin as a triboelectric layer and hollow AgNWs as an electrode layer. RSF exhibits electron-donating properties similar to other natural polymers used in energy harvesting. However, its brittleness limits its use in skin-interfaced applications due to insufficient β -crystallites in its predominantly α -helix and random coil structures. Glycerol addresses this limitation by inducing α -helix and random coil transitions to β -sheet, enhancing mechanical properties through increased β -crystallites. A mixture of RSF solution with 0.1 drops mL⁻¹ of glycerol and polyurethane produces silk fibroin film (SFF) with a fracture strength of 5 MPa at an elongation at break of 520%.

Benchtop studies confirmed the device's electrical output performance, durability, and tactile sensing capabilities. For electrical output measurements, a linear motor applied a cyclic contact to the device. The device (1 \times 1 cm² area) generated 13 V V_{oc} , 0.4 μ A I_{SC} , and 1.7 nC Q_{SC} at 1 Hz operation. The device achieved maximum power of 0.8 W m^{-2} at 600 $M\Omega$ load across 10 $M\Omega$ to 2 $G\Omega$ loads. Durability tests demonstrated consistent performance over 7500 cycles at 1.5 Hz frequency. A larger device $(2 \times 2 \text{ cm}^2)$ area) integrated with a full-wave rectifier charged a 1 μF capacitor to 3.1 V within 135 s at 3 Hz contact frequency, providing sufficient energy to operate a digital watch for ≈ 5 s. For tactile sensing, a 3×3 array of 1×1 cm² devices detected a diagonal pressure pattern, with seven sensors responding to rectangular acrylic plate placement from upper right to lower left corner. Furthermore, an IoT drone control system, comprising seven devices and a Wi-Fienabled microcontroller, demonstrated forward, backward, left, right, up, down, and clockwise rotation movements.

Bioresorbability studies in various solutions at 25 °C showed that the device dissolved within 96 h in 10% papain solution or

4.7% table vinegar solution, while showing minimal degradation in water. This differential degradation stems from the solutions' ability to disrupt the SFF protein structure.

4.2.2. Chemical Energy Harvesters

A pencil-paper-based chemical energy harvester generates an electrical potential through ambient moisture-induced ion gradients.^[3] The device includes two pencil-drawn interdigital electrodes on polarized paper. The paper, polarized by a moisture-induced polarization process, ^[92] contains a gradient of oxygencontaining groups (e.g., hydroxyl groups, carboxyl groups) on the cellulose fibers between the electrodes. These groups produce a hydrogen ion gradient upon moisture absorption, driving ion diffusion that creates an electrical potential difference between electrodes. Decreasing ambient moisture levels triggers hydrogen ion recombination, restoring the initial state. Repeated pencil traces of the electrode pattern ensure sufficient conductivity. The device could potentially achieve bioresorbability through replacement of conventional paper with water-soluble paper.

Benchtop analysis characterized the harvester's electrical performance. The harvester with a 0.87 cm² active area generated a 480 mV $V_{\rm oc}$ with a 10 M Ω load under 95% relative humidity exposure. These results are comparable to humidity energy harvesters based on advanced functional materials such as graphene oxide^[92] and polyelectrolyte membranes.^[93] The harvester generated an 8 μ A $I_{\rm SC}$ with a 10 Ω external load. Five parallel-connected devices achieved 2.1 V peak $V_{\rm oc}$ and 32 μ A $I_{\rm SC}$. To demonstrate practical applications in healthcare, eight parallel-connected devices operating at 95% relative humidity (RH) established sufficient power for an iontophoretic transdermal drug-delivery system. Fluorescent imaging confirmed successful delivery of Rhodamine B dye from a poloxamer 407-based hydrogel to pig skin.

Bioresorbable TENGs enable continuous monitoring functionality without batteries, eliminating the flexibility constraints and lifetime limitations inherent to battery-powered systems. However, they exhibit notable performance variations despite using the same plasticizer. RSF-based TENGs^[38] demonstrate the highest stretchability (520% elongation), followed by CS devices^[39] with moderate flexibility (87% elongation), while SA systems^[37] exhibit the lowest mechanical performance (48% elongation). SA films^[37] show rapid dissolution in aqueous media (complete degradation within 4 min), while both CS^[39] and RSF^[38] materials require specialized enzymatic solutions (pepsase, papain) or vinegar for degradation (30–96 h).

4.3. Sensing Systems

Bioresorbable sensors address bacterial infection risks during device removal and e-waste accumulation through their transient properties. These sensors employ physical or chemical detection mechanisms. Physical sensors measure capacitance,^[7,8] resistance,^[9,10] and physiological electrical signals.^[11–13] Chemical sensors detect target molecules through fluorescence^[14] or colorimetric changes.^[15,16] **Table 4** summarizes the bioresorbable sensing systems in terms of their target applications, sensing mechanisms, sensing parameters, and constituent bioresorbable materials and components.



www.advelectronicmat.de

 Table 4. Summary of bioresorbable sensing systems.

Гуре	Target application	Sensing mechanism	Sensing parameters	Bioresorbable materials	Bioresorbable parts
Physical	PWV measurement ^[7]	Capacitive pressure sensing	Sensitivity 0.76 \pm 0.14 kPa ⁻¹ (<2 kPa) 0.11 \pm 0.07 kPa ⁻¹ (2–10 kPa)	PHB/PHV	Encapsulation layer
				PVA	Adhesive layer
				Fe-Mg	Electrode
				PGS	Dielectric film
	Physiological response monitoring ^[8]		Sensitivity $0.86 \pm 0.16 \text{ kPa}^{-1}$	Leaf skeleton	Electrode
				Dried-leaf	Dielectric layer
	Physiological vibration, pulse, and motion monitoring ^[9]	Resistive strain sensing	Gauge factor 502	Nose film (PVA, acrylic ester, propylene glycol, phenoxyethanol, Octoxynol-10, benzyl alcohol)	Sensor substrate layer
	Wound monitoring ^[10]	Resistive temperature sensing	Temperature-dependent resistance characteristics 79.9 k Ω at 30 °C 80.5 k Ω at 37 °C $\gamma = e^{11.37-0.00583x} + 0.0001x^2$	PA	Encapsulation layer
			x : temperature [°C] y: resistance [Ω]		
				SiN_xO_y/Si_3N_4	Encapsulation layer
				Мо	Temperature sensor Interconnects
				Ti	Adhesive layer
	PWV measurement Pressure/temperature monitoring, Surface texture recognition[11]	Piezoelectricity Pyroelectricity	Piezoelectric coefficient d_{33} 24pC N^{-1} Pressure sensitivity $41 \text{mV Pa}^{-1} (<2 \text{Pa})$ $1 \text{mV Pa}^{-1} (40-100 \text{Pa})$ $0.026 \text{mV Pa}^{-1} (0.1-100 \text{kPa})$ Pyroelectric coefficient $13 \mu \text{C m}^{-2} \text{K}^{-1}$ Temperature sensitivity $2.6 \mu \text{A m}^{-2} \text{K}^{-1}$	Gelatine	Microdome piezoelec- tric/pyroelectric layer
	Artery pulse and motion monitoring ^[12]	Piezoelectricity	Piezoelectric coefficient d_{33} 8 pC N ⁻¹ Pressure sensitivity 13.2 mV kPa ⁻¹	PLLA/Gly	Piezoelectric film layer
	Iontronic skin electrode ^[13]	Ionic conduction	Conductivity 10^{-2} S m^{-1} Impedance $10^5 \Omega (10 \text{ Hz})$	SBMA ₄₀ -CCS ₁ -Gly ₂	Skin electrode
Chemica	Glucose monitoring ^[14]	Glucose-induced fluorescence	Normalized fluorescence intensity (a.u.) with glucose concentration $4.18 \ at \ 100 \ mg \ dl^{-1}$ $5.71 \ at \ 300 \ mg \ dl^{-1}$	Silk fibroin	MN array
				GF-monomer	MN array
				PVA	MN backpacking layer
	COVID-19 antibody detection ^[15]	Immunochromatography	LoD of IgM 3 ng mL ⁻¹ LoD of IgG	Porous PLA	MN array

(Continued)





www.advelectronicmat.de

Table 4. (Continued)

Туре	Target application	Sensing mechanism	Sensing parameters	Bioresorbable materials	Bioresorbable parts
	Sweat analysis ^[16]	Sweat colorimetry	Distance metric $\Delta E \cdot ab$ from the CIELAB color space pH 4.5: 52 pH 7.0: 30 ($R^2 = 0.985$) 25 mM chloride: 50 100 mM chloride: 42 ($R^2 = 0.982$)	Cellulose	Encapsulation layer
				TPC	Sweat-collecting microstructure
				Acrylic PSA	Adhesive layer

4.3.1. Physical Sensors

Recent bioresorbable skin-mounted physical sensors operate through three primary mechanisms: capacitive sensing between parallel plates with pressure-sensitive dielectric materials, [7,8] resistance changes in piezoresistive [9] or thermoresistive materials, [10] and detection of physiological electric signals via piezoelectric materials [11,12] or specialized electrodes. [13]

4.3.2. Capacitive Sensors

A bioresorbable capacitive pressure sensor enables pulse wave velocity (PWV) measurements through a patch-type design.[7] The device architecture (Figure 8a) is built upon a core PGS dielectric film (150-µm-thick) micropatterned with square pyramids (2-µm height, 4-µm base width) for pressure-sensitive capacitance modulation. This sensing layer is sandwiched between Fe-coated (2-nm-thick) Mg electrodes (100-µm-thick)—5 vertical electrodes above and 4 horizontal electrodes belowwhich are embedded in PVA adhesive layers, forming a 4 × 5 capacitive sensor array (each $2.42 \times 2.42 \text{ mm}^2$). Two polyhydroxybutyrate/polyhydroxyvalerate (PHB/PHV) films provide outer encapsulation, each bonding to its corresponding PVA adhesive layer. The pyramid-patterned PGS provides a fast response time and high reproducibility through its minimal viscoelasticity.[58,94,95] Device sensitivity and detection range can be tailored by modifying the pyramidal microstructures: tuning their mechanical properties (e.g., elongation at break, Young's modulus), height, and spatial density in the film.[96,97]

Benchtop studies demonstrated the device's sensitivity, response time, repeatability, and flexibility. The pressure sensor patch incorporating 20 capacitors exhibits a sensitivity of $0.76\pm0.14~\rm kPa^{-1}$ at <2 kPa and $0.11\pm0.07~\rm kPa^{-1}$ at 2–10 kPa. The microstructured PGS film reduces response time from tens of seconds to milliseconds compared to flat film configurations without pyramidal patterns. Cyclic loading tests (8000 cycles, 80 kPa pressure, 4 s periods) demonstrated minimal hysteresis and stable performance, with capacitance increases of 16% and 4% under no pressure and maximum pressure (80 kPa), respectively, and pressure sensitivity changes below 10%. Bending tests at 27 mm radius revealed sensitivity decreases of 10% and 20% in the 5–10 kPa and 0.1–2 kPa ranges, respectively. These sensitivity changes remain acceptable for arterial pulse monitoring and PWV measurements. To evaluate lower pressure detection capa-

bilities, lightweight object mapping tests demonstrated successful detection and localization of a 5 mg single grain, a 21.8 mg rice grain, and a 22.5 mg insect, corresponding to pressures as low as 3 Pa.

Arterial tonometry tests validated the device's clinical applicability. The sensors captured characteristic peaks and pulse wave foot when placed above the radial artery on the wrist. PWV measurements required simultaneous ECG recording and two pressure-sensing skin patches: one above the carotid artery and another above the femoral artery. The ECG provided a time reference for both measurements. The time delay between the carotid and femoral pulse signal feet combined with the neck-to-groin distance yielded a PWV of 7.5 m s $^{-1}$, consistent with that of healthy subjects.

In vitro degradation studies validated the device's bioresorbability. As shown in Figure 8a (bottom), the device showed 15% weight loss after seven weeks of immersion in PBS solution at 37 °C. This degradation rate aligns with referenced studies, reporting 17.6% weight loss of PHB/PHV film in PBS after 60 days, $^{[58]}$ and complete degradation of 50-µm-thick PHB/PHV within 10 weeks in soil at 25 °C and 50 weeks in seawater at 15 °C. $^{[98]}$ The metal electrode layer (Mg and Fe) showed the fastest degradation among the device components upon PBS penetration through the PHB/PHV film.

A bioresorbable capacitive pressure sensor facilitates facial expression, exhalation, vocal chord vibrations and motion monitoring by employing natural leaf architectures (Figure 8b). [8] The leaf-mimetic device incorporates two electrodes that sandwich a dielectric layer, as shown in Figure 8b. Two *Ficus elastica* leaf skeletons form the electrodes, with a hybrid network of oxidized single-walled carbon nanotubes (Ox-SWCNTs) and AgNWs coating their surface. A dried *Prunus avium* leaf functions as the dielectric layer between these electrodes. A cellulose tape encapsulates the whole device.

Benchtop studies evaluated the device's electrical/mechanical properties, pressure sensitivity, robustness, transparency, permeability, and bioresorbability. The device with 4 wt% Ox-SWCNT achieves a sheet resistance of 1.02 Ω sq $^{-1}$ and Young's modulus of 1283 MPa. The device demonstrated a sensitivity of 0.86 \pm 0.16 kPa $^{-1}$, with a low limit of detection (LoD) of 10 Pa. The device maintains stable performance through 3000 cycles at 5 and 10 kPa loading under 30–70% humidity exposure. Optical measurements reveal 60% and 62% transmittance for the coated and uncoated (natural) leaf skeletons, respectively, across 350–800 nm wavelengths. The device (0.73-mm-thick) allows water

2199160x, 2025, 10, Downloaded from https

onlinelibrary.wiley.com/doi/10.1002/aclm.202400997 by Chung-Ang University, Seoul, Wiley Online Library on [06/07/2025]. See the Terms

inditions) on Wiley Online Library for rules of use; OA articles are governed by the applicable Creative Common

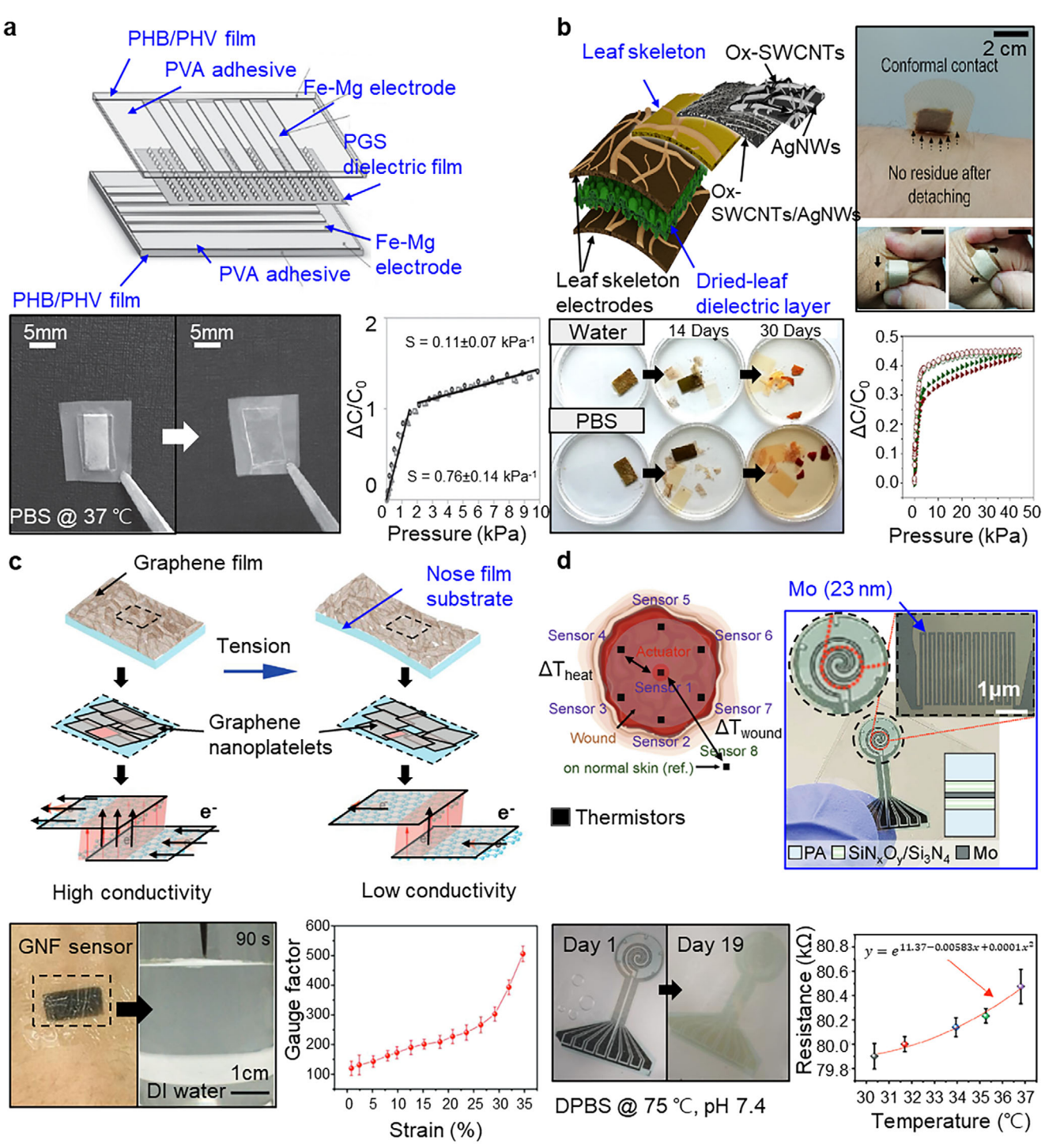


Figure 8. Capacitive and resistive sensors. Bioresorbable materials or devices appear in blue text in the figure. a) Schematic illustration and photograph of capacitive pressure sensor, and photograph of dissolution test, along with sensitivity graph. Reproduced with permission.^[7] Copyright 2015 Wiley-VCH GmbH & Co. KGaA. b) Schematic illustration and photograph of leaf-based capacitive sensor, and photograph of dissolution test, along with sensitivity graph. Reproduced with permission. [8] Copyright 2023 Elsevier B.V. c) Schematic illustration of GNF sensor and its principle with photograph of bioresorption process, along with gauge factor under varying strain. Reproduced with permission. [9] Copyright 2018 Wiley-VCH GmbH & Co. KGaA. d) Schematic illustration of WMS and sensing actuation module, and image of bioresorbable sensing-actuation module with bioresorption process, along with the bioresorbable temperature sensor resistance under varying temperature. Reproduced under the terms of the CC-BY Creative Commons Attribution 4.0 International license. [10] Copyright 2024, Wiley-VCH.



www.advelectronicmat.de

penetration within 6200 ms and bioresorbs in both water and PBS solution.

Various physiological activities generate localized pressure changes throughout the body. The leaf-mimetic capacitive sensors mounted on multiple body locations enabled detection of these pressure variations. Eyelid and forehead-mounted devices exhibited signal acceleration proportional to blinking and frowning speeds. For joint motion analysis, devices attached directly to the index finger knuckle, elbow, and knee demonstrated corresponding signal patterns with increasing amplitudes at greater bending angles (45°, 60°, 90°). Additional devices mounted on the heel and wrist successfully captured cyclic pressure patterns during walking and wrist flexion, respectively. Mask-mounted devices detected simulated breath pressure variations (100 Pa, 200 Pa) generated by nitrogen gas pulses, and captured vocal cord vibrations during pronunciation of "Home."

4.3.3. Resistive Sensors

A graphene nose film (GNF) sensor integrates a piezoresistive graphene layer (200-nm-thick) with a bioresorbable commercial nose film (20-µm-thick) for vibration and pulse monitoring, and HMI applications, ^[9] as shown in Figure 8c. The device consists of a piezoresistive graphene film composed of fish-scale graphene nanoplatelets, laminated on a nose film substrate. The graphene nanoplatelets overlap with each other on the nose film substrate, creating conductive pathways through these overlapping regions. When the sensor experiences strain, the overlapping area between adjacent nanoplatelets decreases, reducing the conductivity of the pathways. ^[99] This mechanism converts applied pressure into measurable changes in resistance. The strong adhesion of the nose film substrate enables the GNF sensor to exhibit a peeling force of 29.4 N m⁻¹.

Mechanical characterization employs a GNF sensor with an $18 \times 8 \text{ mm}^2$ graphene film laminated on a $30 \times 10 \text{ mm}^2$ nose film substrate. The normalized relative resistance increased exponentially with external tensile strain ranging from 0.8% to 35%, yielding gauge factors of 120-502, comparable to existing strain sensors. [99–102] The device exhibited a stretchability of 20– 30% similar to the human skin,[103] and maintained its resistive response through 1000 cycles under 20% strain, with a 54 ms response time. For physiological monitoring, a smaller GNF sensor $(20 \times 10 \text{ mm}^2 \text{ substrate}, 12 \times 6 \text{ mm}^2 \text{ rectangular graphene})$ pattern) captured various vibrations from multiple body sites, including the neck, the jugular vein, and the radial artery. On the neck, it distinguished swallowing, coughing, and saving "hello" with good reproducibility, capturing peaks and valleys generated by muscle movements and effectively detecting the jugular venous pulse. On the wrist, the device enabled radial artery pulse monitoring. For HMI applications, four GNF sensors (20 × 8 mm² substrate, 15 × 6 mm² graphene pattern) mount on four fingers to translate finger bending motions into four-directional bar movements (up, down, left, and right) on the display.

The sensor maintains constant resistance at low (33% RH) and medium (52% RH) humidity. High humidity (97% RH) increases resistance through moisture-induced volume changes, but the device recovers upon drying. In vitro testing, as shown in Figure 8c (bottom), showed that a GNF sensor ($15 \times 8 \text{ mm}^2 \text{ sub-}$

strate, $10 \times 8 \text{ mm}^2$ graphene pattern area) dissolves in DI water within 90 s, with dissolution rate increasing linearly with water temperature at 1.02 µg s⁻¹ °C⁻¹.

A wound monitoring system (WMS, Figure 8d) enables real-time wound healing tracking through injured skin temperature and thermal conductivity measurements.^[10] The system integrates a sensing-actuation module (one actuating resistor and eight thermistors), a Bluetooth Low Energy (BLE) SoC, and a battery/WPT power module. The sensing-actuation module employs a strategic arrangement of eight thermistors on the skin-interfacing surface: a central thermistor and six thermistors in a hexagonal pattern (3 mm from the center) on injured skin, and one reference thermistor on healthy skin. The BLE SoC supplies pulsed current to the actuation resistor to generate heat, while surrounding thermistors monitor heat propagation, with temporal-spatial temperature patterns indicating tissue healing status.

The WMS monitors wound healing by measuring exothermic activity via wound temperature differentials ($\Delta T_{\rm wound}$) and scar formation via thermal conductivity, assessed through temperature gradients ($\Delta T_{\rm heat}$) between heated and reference sensors. Lower $\Delta T_{\rm heat}$ indicates higher conductivity. In vivo tests on control and wounded mice showed near-zero $\Delta T_{\rm wound}$ and stable $\Delta T_{\rm heat}$ (\approx 6 °C) in controls. Wounded mice exhibited positive $\Delta T_{\rm wound}$ for 10 days, turning negative as healing progressed. $\Delta T_{\rm heat}$ increased from 5 to 6.5 °C, reflecting an initial rise in conductivity due to biofluid saturation, followed by a decline as scar tissue formed—correlating with visual scar onset between days 7 and 10.

A bioresorbable version of the sensing-actuation module employs Mo traces (23-nm-thick for thermistors, 223-nm-thick for interconnects) sandwiched between $\mathrm{SiN_xO_y/Si_3N_4}$ layers (5-µm-thick), encapsulated in PA (1-mm-thick) layers, as shown in Figure 8d. In DPBS (75 °C, pH 7.4), the Mo traces dissolved within 19 days. Three approaches extended the trace lifetime: a polybutanedithiol 1,3,5-triallyl-1,3,5-triazine-2,4,6(1H,3H,5H)-trione pentenoic anhydride (PBTPA) protective layer (200-µm-thick) extended to 24 h, a beeswax-candelilla layer (200-µm-thick) further extended to 300 h, and increasing Mo thickness extended dissolution time.

4.3.4. Electrical Signal Sensors

A fully bioresorbable ferroelectric gelatine skin sensor enables PWV measurement, pressure/temperature mapping, and surface texture recognition. The sensor (Figure 9a) incorporates two ferroelectric polarized gelatine films with microdomes (8-µm diameter, 15-µm pitch, and 4-µm height) sandwiched between Mg electrodes (600-nm-thick). Two nonpolarized planar gelatine films (10-µm-thick) form the outer encapsulation layer. The microdomes create an interlocked structure, similar to biological skin, which increases charge carrier density by concentrating thermal strain and mechanical stress at the interlocked surfaces. Glutaraldehyde cross-linking enhances ferroelectricity while providing moisture stability up to 70% RH.

Benchtop studies demonstrated the sensor's piezoelectric and pyroelectric performance. The piezoelectric pressure sensitivity exhibited 41 mV Pa⁻¹ below 2 Pa, 1 mV Pa⁻¹ at 40–100 Pa, and



www.advelectronicmat.de

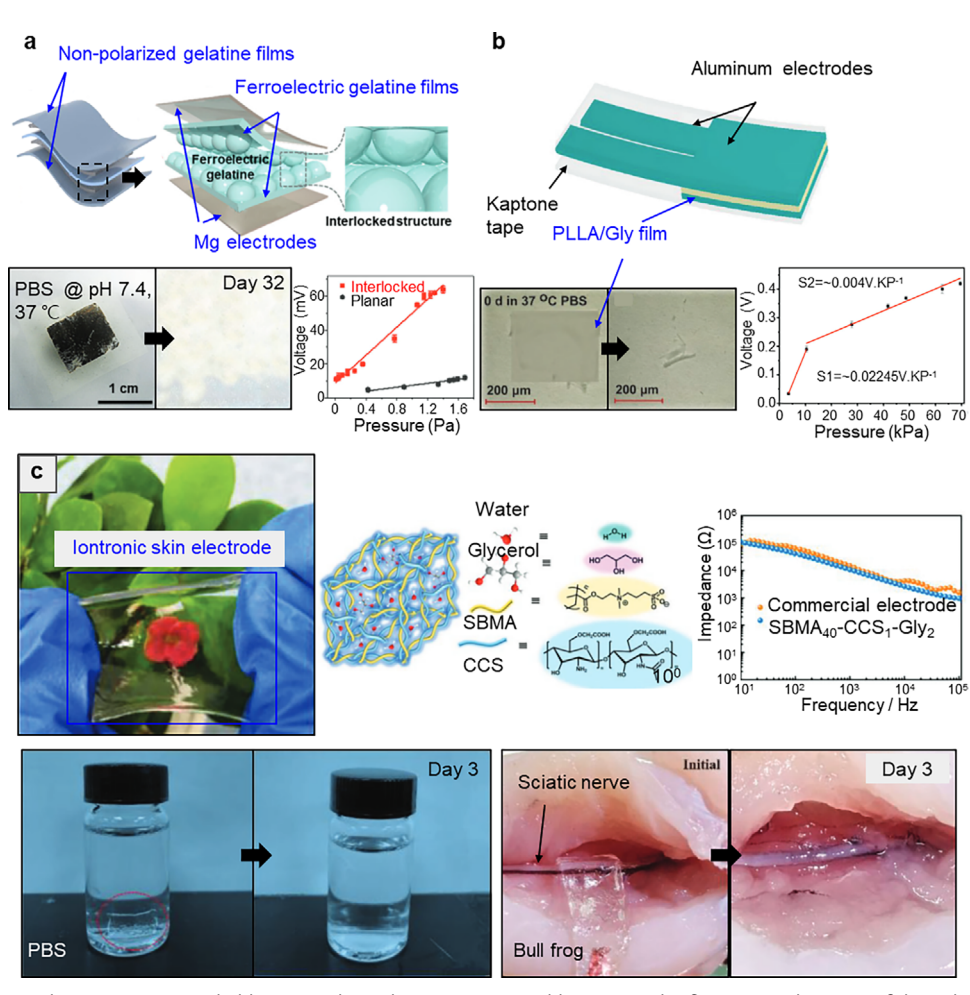


Figure 9. Electrical signal sensors. Bioresorbable materials or devices appear in blue text in the figure. a) Schematic of the gelatine skin sensor and photographs of bioresorption process, along with pressure sensitivity graph. Reproduced under the terms of the CC-BY Creative Commons Attribution 4.0 International license.^[11] Copyright 2021, Wiley-VCH. b) Schematic illustration of film-type device, and photographs of bioresorption process, along with pressure sensitivity graph. Reproduced with permission.^[12] Copyright 2023, Wiley-VCH GmbH. c) Photograph of iontronic skin electrode, schematic illustration of the chemical networks, and photographs of bioresorption process in PBS and in bull frog. Reproduced with permission.^[13] Copyright 2023, Wiley-VCH GmbH.

0.026 mV Pa $^{-1}$ at 0.1–100 kPa with 0.005 Pa LoD. The sensor achieved a piezoelectric coefficient (d $_{33}$) of 24 pC N $^{-1}$ and generated electrical outputs of 2.3 V $V_{\rm oc}$ and 8.9 nA cm $^{-2}$ $I_{\rm SC}$ under 113 kPa pressure. For pyroelectric performance, the sensor exhibited temperature sensitivity of 2.6 μ A m $^{-2}$ K $^{-1}$ and pyroelectric coefficient of 13 μ C m $^{-2}$ K $^{-1}$. The temperature LoD reached 0.04 K, lower than conventional PZT (0.4 K). Temperature variations of 1.8 K at 0.4 K s $^{-1}$ generated a 0.46 nA cm $^{-2}$ pyroelectric current, while maintaining stability over 1300 temperature cycles.

The sensor demonstrated versatile physiological signal detection. On the philtrum, the sensor detected HR (62 bpm) and breathing patterns with 6 K temperature changes, consistent with infrared camera measurements and previous studies. [106,107] Multisite pulse wave measurements from thyroid, carotid, and radial arteries enabled cardiovascular monitoring. Thyroid pulse waveforms revealed cardiovascular responses (HR, augmentation index, and reflection index) during hot and cold water intake, while carotid-radial PWV measurements (5.8 m s $^{-1}$) aligned with clinical standards. [108] The sensor differentiated activity states (rest-

ing, exercising, and sweating) and throat movements (swallowing, coughing, and drinking). A 5 \times 5-pixel sensor array demonstrated pressure (0–7 kPa) and temperature (25–31 °C) monitoring capabilities during hand contact. For surface texture recognition, the device incorporated a fingerprint-like pattern (500- μ m grating period) on the upper layer, enhancing surface sensing capability.

In PBS (pH 7.4, 37 °C), the Mg electrodes degraded within 3 days through water-induced corrosion. ^[109] The sensor maintained structural integrity until day 17 before complete biodegradation by day 32.

Another flexible film-type device enables artery pulse and body movement monitoring through piezoelectric signals. [12] The device comprises a bioresorbable piezoelectric PLLA/Gly layer (15- μ m-thick) between non-bioresorbable aluminum electrodes, encapsulated with Kapton tape (Figure 9b). Glycine addition (10 wt%) to PLLA enhances piezoelectricity through aligned β -crystals formation. Piezoelectric characterization utilized vibration and impact testing. For vibration testing, an electrodynamic



www.advelectronicmat.de

shaker applied 41 Hz vibration to one end of a fixed $21 \times 8 \text{ mm}^2$ film. PLLA with 10 wt% glycine generated the maximum $V_{\rm oc}$ among tested compositions. For impact testing, the shaker applied dynamic force to the film. At 4.5 N force, the 10 wt% PLLA/Gly film generated 0.42 V $V_{\rm oc}$ and exhibited linear voltage increase with applied force, while pure PLLA film produced only noise. The film demonstrated 13.2 mV kPa $^{-1}$ sensitivity, 10 ms response time, and a d_{33} of 8 pC N $^{-1}$. Dynamic pressure testing (5 Hz, 31.25 kPa) confirmed stable piezoelectric output over 4000 cycles.

The film detected physiological signals across different body locations. Radial artery pulse measurements at wrist generated 700 mV $\rm V_{pp}$ with an HR of 72 bpm, revealing two characteristic peaks (P $_{1}$ and P $_{2}$). P $_{1}$ represents systolic–diastolic pressure difference, while P $_{2}$ indicates the difference between the combined travelling-reflected wave peak and diastolic blood pressure. The measured time difference between peaks ($\Delta T_{\rm DVP}$) of 1.05 s and radial augmentation index (AI $_{\rm r}=\rm P_{2}/P_{1}$) of 0.15 matched normal values for subjects under 30 years, $^{[110]}$ indicating arterial stiffness. $^{[111]}$ The film captured carotid artery pulse (400-mV V $_{\rm pp}$) at the neck, distinct esophageal signals during throat movements (coughing, drinking, and swallowing), and joint motions at the wrist and the elbow.

While aluminum electrodes and Kapton encapsulation provided durability and flexibility, biodegradation remained limited to the PLLA/Gly layer. In accelerated testing (PBS, 37 °C, pH 12), the PLLA/Gly film completely dissolved within 5 days, addressing PLLA's slow degradation rate.^[112]

Bioresorbable iontronic skin electrodes represent another approach to transient electrophysiology measurements.[13] The single-layered, patch-type electrode comprises carboxylated chitosan (CCS), sulfobetaine methacrylate (SBMA), and a mixture of glycerol and water, as shown in Figure 9c. CCS and SBMA form distinct networks, while glycerol and water molecules create bridge-like connections between these networks through hydrogen bonds.[113,114] CCS is an amphoteric polyelectrolyte, which provides high ionic conductivity by ionizing and releasing hydrogen ions from its carboxylic acid groups. SBMA enhances adhesion to other interfaces through electrostatic attraction, cation– π interaction, and ionic dipole interaction. Glycerol– water mixture stabilizes the network and softens the material by suppressing water vapor evaporation, while also enhancing charge transfer through carboxylic acid group ionization. The optimized electrode composition (SBMA₄₀-CCS₁-Gly₂) exhibits optimal ionic conductivity (10⁻² S m⁻¹), skin contact impedance (10⁵ Ω at 10 Hz), Young's modulus (1 \pm 0.1 MPa), and maximum strain at break (380% \pm 25%). These properties enable effective electrical signal measurements while providing skin-like mechanical properties and sufficient robustness.

The iontronic skin electrode demonstrated superior performance compared to conventional Ag/AgCl electrodes in measuring various physiological signals. It maintained clear ECG signals under varying humidity (20–80%). Adhesion tests using a vibrator placed 1 cm away from the electrodes showed stable ECG signals from the skin electrode while Ag/AgCl electrode signals degraded. The electrode captured EMG signals with comparable signal-to-noise ratio (SNR) of 42.5 dB to Ag/AgCl electrodes (42.0 dB), enabling robotic hand control through three arm muscle electrodes. Electrooculogram measurements from eye-

lid and cheek electrodes distinguished various eye movements, while EEG alpha waves (8–9 Hz) from forehead electrodes detected tensed states. In vivo experiments on bull frog sciatic nerve demonstrated neural recording capabilities with voltage-dependent action potentials.

In vitro and in vivo experiments confirmed the electrode's bioresorbability. The electrode exhibited 40% mass loss in DI water at room temperature over 3 days and completed dissolution in PBS solution due to structural electrostatic disruption. In vivo implantation on bull frog sciatic nerve demonstrated complete degradation within 3 days.

4.3.5. Chemical Sensing Systems

Chemical sensing systems employ diverse detection mechanisms for specific analyte monitoring. Various sensors utilize different chemical and physical changes, such as glucose-induced fluorescence,^[14] antibody-immunocomplex colorimetric shifts,^[15] and pH-dependent color variations in anthocyanins and silver chloranilate–polyhydroxyethyl methacrylate (pHEMA) systems.^[16]

A bioresorbable fluorescent MN system enables continuous glucose monitoring through fluorescence intensity measurements.[14] The system consists of two main components: an MN glucose sensor and a smartphone-based detector. The sensor $(7 \times 7 \text{ mm}^2)$, shown in Figure 10a, comprises a bioresorbable silk needle layer with 100 MNs (650-µm height) and a PVA backpacking layer. The MNs integrate silk fibroin with glucose-responsive fluorescent monomer (GF-monomer), which emits 490 nm light under 405 nm excitation when exposed to interstitial fluid (ISF). Silk fibroin immobilizes GF-monomers while maintaining their accessibility to ISF. The PVA backpacking layer secures the MNs and facilitates skin insertion. The smartphone-based detector integrates a 405 nm LED array for MN excitation and a 450 nm long-pass optical filter that selectively transmits wavelengths above 450 nm, eliminating interference from excitation light. The smartphone application processes sensor images to extract pure 490 nm emission intensity by removing ambient light, converts the intensity to glucose concentration, and provides data plotting and storage capabilities.

In vitro tests evaluated the continous glucose monitoring (CGM) system response to glucose concentrations ranging from hypoglycemic state (50 mg dl $^{-1}$) to hyperglycemic state (450 mg dl $^{-1}$) under 405 nm light excitation (230 $\mu W\ mm^{-2}$). The system demonstrated a 36.3% fluorescence increase across this range, with a maximum measurement error of 3.4% over 10 repetitions. In vivo validation used three CGM systems on different mice while measuring tail blood glucose with a glucometer every 3 min. The 2–3 h of monitoring revealed two distinct phases: an increase after glucose administration and a decrease following insulin injection. The normalized fluorescence change from all three CGM systems traced the glucose concentration from 40 to 280 mg dl $^{-1}$. The sensor fluorescence gradually decreased with degradation until complete dissolution after 3 days.

Degradation tests in PBS solution (60 °C, pH 4.01) revealed sequential decomposition of the CGM system. The PVA backpacking layer dissolved first, followed by the silk fibroin in MNs, and

2199160x, 2025, 10, Downloa

onlinelibrary.wiley.com/doi/10.1002/aelm.202400997 by Chung-Ang University, Seoul, Wiley Online Library on [06/07/2025]. See the Terms

ions) on Wiley Online Library for rules of use; OA articles are governed by the applicable Creative Commons

www.advancedsciencenews.com

www.advelectronicmat.de

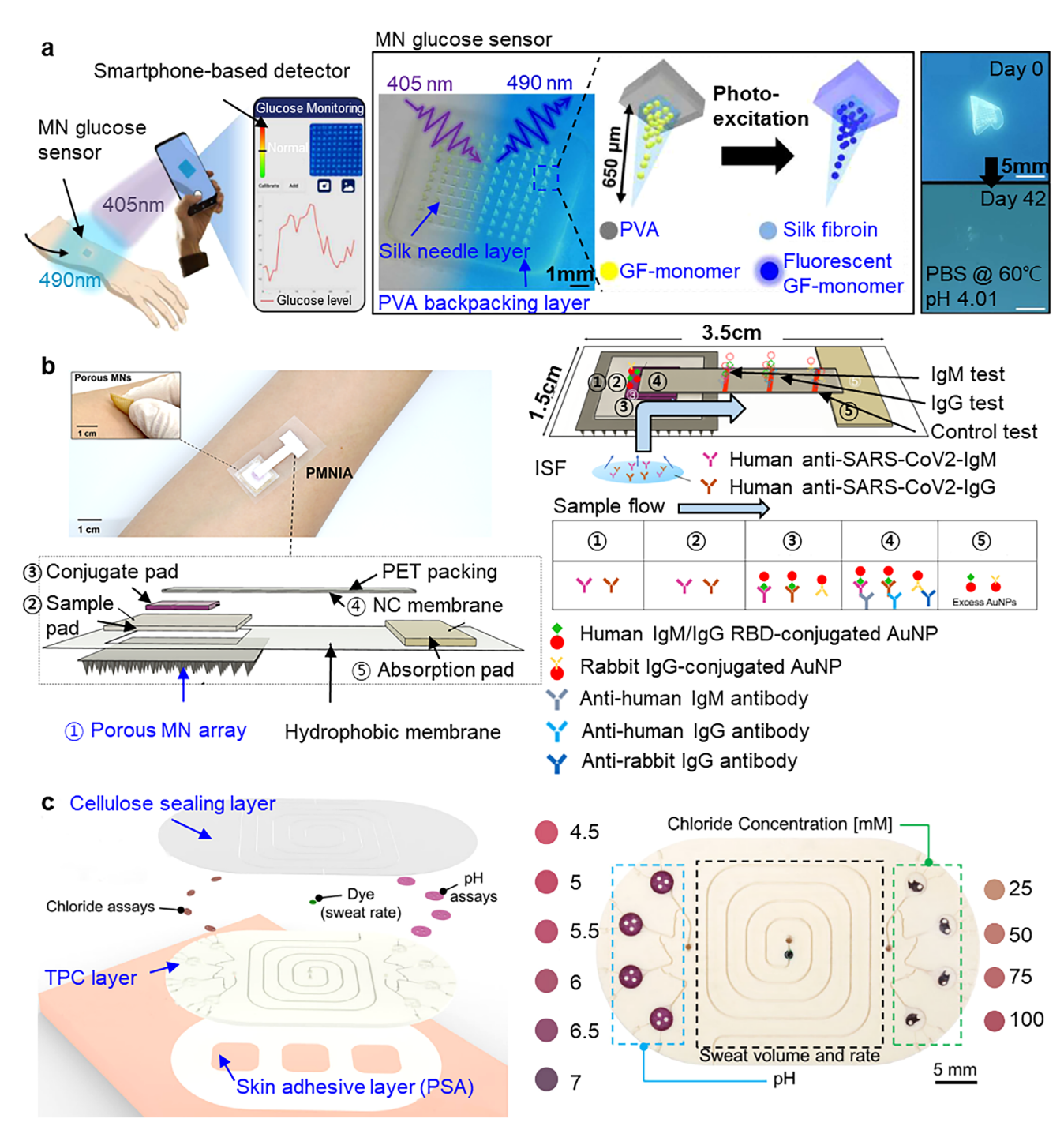


Figure 10. Chemical sensing systems. Bioresorbable materials or devices appear in blue text in the figure. a) Illustration of the glucose monitoring system, photograph of MN glucose sensor with illustration of MN, and photographs of bioresorption test. Reproduced with permission.^[14] Copyright 2023, The American Association for the Advancement of Science. b) Photograph and illustration of COVID-19 antibody detection system. Reproduced under the terms of the CC-BY Creative Commons Attribution 4.0 International license.^[15] Copyright 2022, Nature Portfolio. c) Illustration and photograph of microfluidic device. Reproduced under the terms of the CC-BY Creative Commons Attribution 4.0 International license.^[16] Copyright 2023, Wiley-VCH.

finally the GF-monomer was released, reaching complete bioresorption at day 42. A gelatin skin model prepared with 10 wt% gelatin in glucose solution (100 mg dl $^{-1}$) evaluated the MN resorption, showing MN height reduction from 650 μm to 400–450 μm within 3 days.

A bioresorbable MN patch enables COVID-19 antibody detection through ISF sampling. [15] The system (1.5 \times 3.5 cm²), shown in Figure 10b, consists of six main components: a porous PLA MN array (13 \times 13 array, 1.5 \times 1.5 cm²), a hydrophobic membrane (1.5 \times 3.5 cm²) with a 1 \times 1 cm² hole, a sample pad



www.advelectronicmat.de

 $(1 \times 1 \text{ cm}^2)$, a conjugate pad, a nitrocellulose (NC) membrane with a transparent PET sheet, and an absorption pad. The ISF flows vertically from the MN array through the sample and conjugate pads to the NC membrane, then laterally through the NC membrane, where immunochromatographic assay detects anti-SARS-CoV-2 immunoglobulin M (IgM) and immunoglobulin G (IgG) antibodies. The absorption pad collects excess fluid to maintain continuous flow. This system provides a minimally invasive alternative to conventional testing methods, including nasopharyngeal sampling and blood-based antibody testing. IgM antibody levels peak within 3 weeks after symptom onset, while IgG antibody levels peak between 3 and 8 weeks and remain elevated. These distinct antibody profiles indicate both infection status and progression.

The porous PLA MN array extracts the ISF through interconnected pores via capillary action. A 30-min heat treatment (180 °C) of PLA and PVA emulsion creates these porous MNs, simplifying conventional porogen leaching methods.[116-118] The conjugate pad contains two types of gold nanoparticles (AuNPs): spike protein receptor binding domain (RBD)-conjugated AuNPs for IgM/IgG antibodies binding, and rabbit IgG-conjugated AuNPs. The NC membrane contains three types of immobilized antibodies at different positions: anti-human IgM antibodies, anti-human IgG antibodies, and anti-rabbit IgG antibodies. As ISF flows through the membrane, anti-human IgM antibodies capture RBD-conjugated AuNP-IgM complexes while antihuman IgG antibodies capture RBD-conjugated AuNP-IgG complexes, forming reddish-purple lines visible through the transparent PET sheet. The anti-rabbit IgG antibodies capture rabbit IgG-conjugated AuNPs, serving as a flow indicator.

Antibody detection tests used four 80- μ L antibody solutions: anti-SARS-CoV-2 IgM antibody (0.5 μ g mL⁻¹) solution, anti-SARS-CoV-2 IgG antibody (0.5 μ g mL⁻¹) solution, mixed anti-SARS-CoV-2 IgM/IgG antibodies solution (0.5 μ g mL⁻¹ each), and PBS solution as control. The IgM solution generated lines at the anti-human IgM antibody and the control position, while the IgG solution generated lines at the anti-human IgG antibody and control positions. The mixed solution generated lines at all positions. The PBS solution generated only the control line, confirming proper fluid flow. The IUPAC standard method determined the LoD as 3 ng mL⁻¹ for IgM antibodies and 7 ng mL⁻¹ for IgG antibodies. [119]

A soft, environmentally degradable microfluidic device enables colorimetric sweat analysis. [16] The skin-interfaced device (Figure 10c) collects sweat through microfluid channels to measure sweat rate and total sweat loss. The device integrates four layers: a cellulose sealing layer (45 µm in thickness), thermoplastic copolyester elastomer (TPC, 750-µm-thick) layer containing microstructures, acrylic pressure-sensitive adhesive layer (PSA, 20μm-thick) bonding cellulose to the TPC layer, and a double-sided commercial skin adhesive layer (150-µm-thick). Sweat flows from the collection area (60 mm²) into microchannels through eccrine gland pressure. The cellulose layer prevents sweat evaporation, showing WVTR of 113 g mm m⁻² day⁻¹ while PDMS shows 382 g mm m^{-2} day⁻¹. [120] The TPC layer contains three microchannels (330-µm-deep): a central channel with green dye for tracking sweat movement for sweat rate and sweat loss calculations, and two side channels connecting to analysis reservoirs (1.8 \pm 0.1 μ L each). The reservoirs analyze chloride concentration through silver chloranilate in pHEMA and pH through anthocyanin indicators, with a CIELAB algorithm converting color changes to concentrations. A commercial skin adhesive with low modulus of 17 kPa ensures conformal skin contact.

The device achieves bioresorbability by incorporating bioresorbable materials: cellulose, acrylic PSA, TPC material, titanium dioxide, and chemical indicators. Cellulose degrades by microorganism enzymes (i.e., cellulases) breaking its β -1,4 glycosidic bonds.[121,122] Acrylic PSA degrades through microorganism hydrolytic enzymatic reactions and aerobic metabolism.[123] The TPC layer combines TPC material and titanium dioxidebased white pigments. The TPC material contains ester bonds that break down and are absorbed by microorganisms.[124] Titanium dioxide undergoes microorganism consumption without bioaccumulation.[125] The chemical indicators inside the TPC layer maintain bioresorbability. Chlorophyll degrades through biometabolism into colorless catabolites without toxic intermediates. Anthocyanin breaks down by microorganism enzymes, such as β -glucosidase, polyphenol-oxidase, and peroxidase, leaving phenolic acids, amino acids, proteins, and quinones, [126,127] and pHEMA degrades by macrophage cell line. [128] Silver chloranilate, though not bioresorbable, maintains overall biodegradability through its low mass content of 0.03 wt%, below the compostability standards criteria.[129]

Recent studies on bioresorbable sensors predominantly report discrete performance-degradation data (e.g., gelatin sensors^[11]: 41 mV Pa⁻¹ sensitivity, 32-day degradation; PLLA/Gly films^[12]: 13.2 mV kPa⁻¹ sensitivity, 5-day degradation) without systematically investigating how modifying degradation rates affects sensing performance. Future research should evaluate sensors with controlled degradation while measuring corresponding changes in sensitivity, stability, and other functional parameters. This would guide material selection and enable application-specific designs for diverse clinical needs.

5. Bioresorbable Transistor Applications

Semiconductor devices such as transistors, capacitors, and diodes consist of a semiconductor, metal, and dielectric layer, which can be facilitated by using bioresorbable materials, as mentioned in previous sections. Transistors, for example, usually amplify or switch electrical signals by controlling sourcedrain voltage, current or gate voltage. These unique features can realize neurophysiologic monitoring devices for diagnosing and treating brain diseases such as Parkinson's disease, pain, epilepsy, etc.[130,131] Capacitors and diodes regulate electric signals by rectifying AC to DC, minimizing noise signals, and modifying pulse width. Additionally, an inductor-capacitor network (LC circuit) presents a WPT system, which can be utilized as a power source inside the body.[132] Physical disappearnce of structures after desired time scales eliminates retrieval processes, and minimize the use of hazardous chemicals for recycling or disposal.

A fully bioresorbable electronic device including a transistor, capacitor, inductor, resistor, diode, interconnect, and substrate was demonstrated in 2012 (Figure 11a).^[44] Physical vapor deposition selectively deposits Mg, MgO, and SiO₂ using stencil shadow masks for components such as inductor, capacitor, resistor, interconnect, dielectric, and transistor. The transfer printing

2199160x, 2025, 10, Downlo

onlinelibrary.wiley.com/doi/10.1002/aclm.202400997 by Chung-Ang University, Seoul, Wiley Online Library on [06/07/2025]. See the Terms

on Wiley Online Library for rules of use; OA articles are governed by the applicable Creative Common

Figure 11. Implantable transistors. a) Schematic illustration of a fully bioresorbable electronic device, including a transistor, capacitor, inductor, resistor, diode, interconnects, and substrate, along with its resorption process. Reproduced with permission.^[44] Copyright 2012, The American Association for the Advancement of Science. b) Schematic illustration of MOSFETs) and the mass production process on silicon-on-insulator wafer, along with the resorption process. Reproduced with permission.^[45] Copyright 2013, Wiley-VCH GmbH & Co. KGaA. c) Schematic illustration of the organic electrochemical transistor along with its resorption process. Reproduced with permission.^[41] Copyright 2023, Wiley-VCH GmbH.

2 week

4 week

technique facilitates control of Si NMs-based transistor and diode position on the substrate. The dissolution rate of Si NM is 4.5 nm day $^{-1}$ at body temperature (37 °C). The functional lifetime of a resistor changes by encapsulation materials and thickness from 2 to 100 h. Metal oxide semiconductor field-effect transistor

(100)

(MOSFET) shows stable operation over 84 h and rapidly loses its function at $\approx\!90$ h; linear regime mobilities of n- and p-channel are 560 and 550 cm² V $^{-1}$ s $^{-1}$, respectively; on/off ratio is $>\!10^5$. These components facilitate strain gauges (gauge factors: $\approx\!40$), a digital imaging system, a wireless power receiving antenna with

1 hr.

Biodegradable Substrate

(PLGA, 12 μm)

90 °C, pH=7.2

original





www.advelectronicmat.de

a resonance frequency of \approx 1.8 GHz, and a wireless implantable heating system for thermal therapy.

Developed configuration of MOSFETs and mass production on silicon-on-insulator (SOI) wafer was presented in 2013 (Figure 11b).[45] Photolithography-based fabrication processes realize wafer-scale fabrication of bioresorbable MOSFETs. Transfer printing facilitates the transfer of MOSFETs onto silk substrates without contamination or deformation caused by lithographic techniques, solvents, temperature, and etchants during the fabrication process. Selective doping (phosphorous at ≈950 °C) to 100-nm thick (100) p-type Si on SOI wafer (a buried oxide layer (≈1-µmthick) and supporting (111) Si wafer) defines the channel and contact regions. Patterned etching of Si wafer generates isolated areas for the MOSFETs. Plasma-enhanced chemical-vapor deposition (PECVD) of SiO₂ and chemical wet etching create gate dielectric layers with open windows for source and drain contact areas. Electron beam deposition of Mg forms source, drain, and gate electrodes. PECVD deposits encapsulation layers of SiO2 and silicon nitride (Si₃N₄). Deep etching and anisotropic wet etching of the (111) Si wafer leave freestanding MOSFETs on a buried oxide layer. Reactive ion etching with sulfur hexafluoride (SF₆) gas removes Si₃N₄ after transfer to silk substrate. These fabrication processes can be applied to logic gates and integrated circuit fabrications. An inverter, for example, has consistent voltage transfer characteristics with gains of up to ≈4 at supply voltages of \approx 5 V when the input voltage is from -2 V to 4 V. NAND and NOR circuits demonstrate "0" and "1" state with output voltage of ≈0.07 V, and ≈2.67 V, respectively. Opened Mg electrodes begin dissolving in PBS (pH 7.4) solution at 37 °C during the first 10 h. Hydrolysis of Mg initiates cracks in the SiO₂ and dissolution in two weeks; Si completely dissolves under 4 weeks. Additional encapsulation strategies such as adding a MgO layer can extend the functional lifetime.

ECoG electrodes for neural interfaces are widely utilized for diagnosing and treating brain diseases such as Parkinson's disease, depression, and disorders of the peripheral nervous system.^[40] Bioresorbable ECoG electrode arrays (256 independent channels) consist of phosphorus-doped Si NMs electrode (300-nmthick), SiO₂ insulation layer (100-nm-thick), and PLGA (30-µm-thick).[133] Electrochemical impedance spectroscopy confirms Si microelectrode has an impedance of $\approx 100 \text{ k}\Omega$ at 1 kHz, which is similar to gold electrode. Owing to the slower dissolution rate of Si NMs (\approx 10 nm day⁻¹) than bioresorbable metals, the ECoG electrode records cortical potentials over 1 month. In vivo studies in adult rat animal models capture electrophysiological signals from the cortex in the left hemisphere. The bioresorbable electrodes are placed next to a control electrode of a standard stainless steel microelectrode (7850 µm²). Both electrodes successfully record the transition to deep anesthesia, K-complexes, pre-ictal, ictal-like spiking epileptiform activities, theta waves, and sleep spindles. In vivo biocompatibility test confirms that the bioresorbable ECoG electrode has a similar biocompatibility as a platinum reference electrode. Active 128 n-channel MOSFETs facilitate high-resolution neural interfaces; Mo electrodes serve as the source, drain, and gate electrodes; the mobility is ≈400 cm² V^{-1} ; on/off ratio is $\approx 10^8$; leakage current is ≈ 10 nA. Somatosensory evoked potential experiments demonstrate potential applications of the bioresorbable active electrodes. Stimulation at two different points evokes potentials in the barrel cortex and other electrodes record stimulus-evoked neural activities with a high SNR.

electrochemical transistor (OECT) other opportunity for next-generation neural interfaces (Figure 11c).[41] Polymer semiconductors, for example, poly(3,4ethylenedioxythiophene):polystyrene sulfonate (PEDOT:PSS), enables low Young's modulus, improve flexibility, and operate in low operation voltage. The dissolution rate of PEDOT:PSS is ≈5.33 µg L⁻¹ day⁻¹. Dry-etching process defines PEDOT:PSS channel geometry. Ultrathin and soft device architecture realizes the conformal contact against the cerebral cortex. Positive gate voltage-induced cations doping on PEDOT:PSS decreases the drain current. The transconductance value (g_m) is the amplification capability of the OECT. The average $g_{\scriptscriptstyle \rm m}$ of the array is 8.67 ± 0.3 mS at a low-frequency range and maintains several milliSiemens below 900 Hz. In vivo animal studies using 4-6 week-old Sprague Dawley rats demonstrate neural activity recording using the OECT. 100 OECTs record the electrophysiological signals under anesthesia, during the epileptic seizure, and with electric stimulation. H&E image confirms the OECT has good biocompatibility without any significant side effects. The OECT electrodes can operate for one week due to the degradation of PEDOT:PSS during in vivo studies.

6. Bioresorbable Implantable Sensor Applications

Temperature, pressure, strain, pH, oxygen level, etc., are critical indicators to monitor patient health conditions and diagnose recovery status. The piezoresistive effect is a mechanical strain-induced electrical resistivity change of semiconductors and metals; temperature is another critical factor in determining the electrical conductivity of semiconductors and metals. Encapsulated air cavity structures, for example, provide pressuresensitive mechanical deformation to Si NM for the piezoresistive change (Figure 12a).[42] Partially square-shape etched (depth: 30-40 µm) nanoporous Si (71% porosity) and PLGA cover membrane present an air cavity. Serpentine geometry Si NM is placed near the edge of the cavity where deflection-induced strains are maximized. The resistance changes of Si NM by the full range of pressure changes (0-70 mmHg) show corresponding results with a commercial pressure sensor; the gauge factor of Si NM is ≈30. Acceleration sensors, temperature sensors, pH sensors, and flow sensors are also potential applications using a similar structure. The dissolution test confirms the dissolution rate of Si NMs (23 nm day⁻¹), and thin nanoporous Si (9 μ m day⁻¹) in artificial cerebrospinal fluid at physiological temperature (37 °C). In vivo experiments demonstrate the measurement of intracranial pressure (ICP) and intracranial temperature in rat models. The ICP measurement results reveal the accuracy of the bioresorbable system is similar to commercial sensors; in vitro test confirms the expected operation time is around 3-7 days depending on the encapsulation layers. Biocompatibility test after 8 weeks of implantation confirms no overt reactions to the sensors and the byproducts. Multifunctional sensors monitor physiological parameters of deep brain pressure and temperature, which are difficult to measure from the surface or the intracranial space; temperature sensors can capture temperature decrease caused by anesthesia and wake-up.



www.advelectronicmat.de

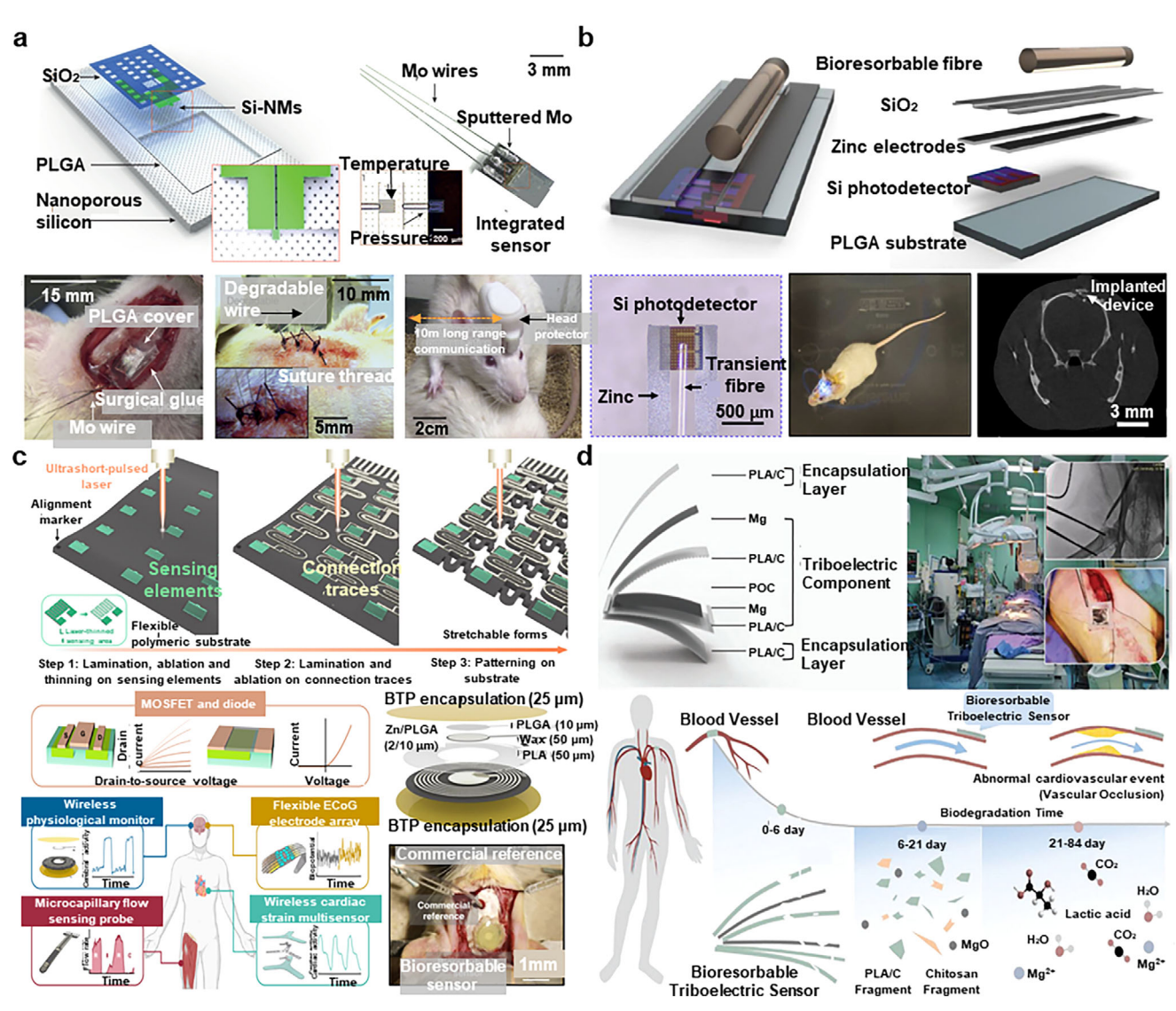


Figure 12. Implantable sensors a) Schematic illustration of encapsulated air cavity structures providing pressure-sensitive deformation to Si nanomembrane for piezoresistive changes. A freely moving rat implanted with a fully bioresorbable wireless intracranial sensor, with the craniectomy sealed using a PLGA film (≈80 μm) and biodegradable surgical glue (TISSEAL). Reproduced with permission. [42] Copyright 2016, Springer Nature Limited. b) Schematic illustration of spectroscopic characterization at visible and near - infrared wavelengths to monitor cerebral temperature, oxygenation, and neural activity in mice. A bioresorbable spectrometer implanted in a freely moving mouse, with axial-view confirmation via computed tomography. Reproduced with permission. [134] Copyright 2019, Springer Nature Limited. c) Schematic illustration of ultrafast pulsed laser ablation enabling the fabrication of high-speed, multilayered electronic systems, including MOSFETs, ECoG arrays, and physiological monitoring systems. A bioresorbable physiological monitoring device mounted over a craniotomy, shown alongside a standard clinical ICP monitor. Reproduced with permission. [43] Copyright 2022, Nature Portfolio. d) Schematic illustration of a biodegradable triboelectric self-powered sensor (BTS) converting biomechanical movement into voltage signals to detect vascular occlusion events. Image of a cardiac monitoring experiment in a human-scale animal model. Reproduced with permission. [135] Copyright 2021, Wiley-VCH GmbH.

Spectroscopic characterization at visible and near-infrared wavelengths provides physical and chemical information on targeted tissues such as cerebral temperature, oxygenation, and neural activity in mice (Figure 12b). [134] A bioresorbable optical system including fully bioresorbable components of tricolor photodetectors, ceramic optical filters, and optical polymer fibers demonstrates that the system can be implanted in deep brain regions for continuous monitoring in vivo. 10 μ m thick PLGA substrate supports 1) a PLGA bioresorbable fiber (150 μ m diameter, refractive index of 1.50) for delivering specific wavelength of

lights, 2) a bioresorbable photodetector (doped monocrystalline Si, 1.5 μ m thick) for generating electrical signals, and 3) Zn electrodes (400 nm thick) for electrical readout. 50 nm thick SiO₂ layer (refractive index: \approx 1.45) encapsulates the system for delaying bioresorbable time and enhancing light confinement inside the fiber. The photodetector consists of insulator, p- and n-doped regions that use comb-like geometries to maximize the depletion region (quantum efficiencies of green and red light are 31.5% and 26%, respectively). The PLGA bioresorbable fiber coats with alginate hydrogel to improve optical performance. The optical





www.advelectronicmat.de

properties of the device decrease on day 3 due to water penetration through the SiO2 encapsulation layer (for the first two days) and degradation of Zn electrodes. Vertically stacked four doped layers (from top to bottom: n-doped A layer, p-doped B layer, n-doped B layer, and p-doped D layer) build n-p (between AB layers), p-n (between BC layers), and n-p (between CD layers) junctions to facilitate a tricolor bioresorbable photodetector. Due to extra layers of A and A, B layer on BC and CD junctions, AB, BC, and CD junctions enable different peak responsivities at 490, 570, and 720 nm wavelength, respectively. The combination of multilayers of SiO_x (54 nm thick) and SiN_y (85 nm thick) placed between top and bottom PLGA layers (10 µm thick) facilitates flexible bioresorbable optical filters designed to block 450-520 nm wavelengths. Hematology and biochemistry confirm no abnormal implantation and accumulation of Si and Zn during 7-week implantation, measured by inductively coupled plasma optical emission spectrometry and inductively coupled plasma mass spectrometry. Biodegradable spectroscopic technology can measure oxygenation level in blood samples and tissue temperature, detect biochemical species (e.g., serum albumin and melanin) and Ca²⁺ concentrations. In vivo experiments present the feasibility of measuring cerebral temperature, oxygen saturation level, and neural activities with minimal inflammatory glial responses.

Ultrafast pulsed laser ablation facilitates the fabrication of high-speed, multilayered electronic systems of MOSFET, wireless physiological monitoring systems, ECoG electrode array, microcapillary flow sensing probe, and cardiac strain multisensor (Figure 12c).[43] The picosecond-pulsed laser ablation yields a minimum effective width of \approx 5 μ m, and root-mean-square (RMS) edge roughness of ≈1 µm of Si NM, respectively. Average power, number of repeats, scanning speed, and frequency control the thickness reduction rate. Repeated ablation produces ≈300-µm-thick Mg microstructure with minimal damage to the underlying layer. A bioresorbable Mg inductor (helical coil thickness: 280 µm and diameter: 4 mm; PLA substrate thickness: 50 um) fabricated by laser ablation method, for example, exhibits RMS surface roughness of $\approx 5 \, \mu m$ and the quality (Q factor) of over 70. The pressure changes around the LC circuit detect ICP with a sensitivity of $\approx 500 \text{ kHz mmHg}^{-1}$, respiration rate (duration: ≈ 0.7 s), and heart rate (duration: ≈ 0.2 s). A flexible needleshaped probe containing three thermistors (resistance of $\approx 650 \,\Omega$, sensitivity of $\approx 3.3 \ \Omega$ °C⁻¹) demonstrates monitoring microvascular flow in soft tissue. In vivo acute evaluations confirm blood flow velocities in various conditions and demonstrate potential capabilities for fast diagnosis related to blood circulation. Multielectrode sensors enable neurophysiological monitoring of brain function using an n-doped Si micromembrane (Si NM, 2-umthick, the impedance of 50–80 k Ω at 1 kHz). In vivo ECoG recording results show sleep spindle activity and optogenetic activation. Si-based n-channel MOSFETs have an effective mobility of 610 \pm 20 cm² S⁻¹ V⁻¹, an on-off current ratio of 700 \pm 120, a threshold voltage of -0.35 ± 0.05 V, and a subthreshold slope of 330 \pm 60 mV decade⁻¹. Multisensing electronic systems measure shear strain, heartbeat, and respiration to diagnose cardiac disorders. The sensitivity to strain-induced changes in resonance frequency is ≈200 kHz strain⁻¹ with negligible bending sensitivity. In vivo evaluations of the multisensing device mounted on the left ventricle acquire respiration rate and heart rate of the anesthetized ovine animal.

Biodegradable triboelectric effect-based self-powered sensor (BTS) converts biomechanical movement into voltage signals to identify vascular occlusion events (Figure 12d).[135] The sensor utilizes a vertical contact-mode TENG that converts mechanical motion into electrical signals, enabling self-powered tactile sensing for implantable applications. The TENG operates based on the coupling of contact electrification and electrostatic induction, where periodic contact and separation between two materials generate an alternating current. Nanostructured poly(lactic acid)-(chitosan 4%) (PLA/C) film and Mg layers realize vertical contact mode TENG that generates 4.2 Voc by contact and separation (contact force: 20 N) and shows stable output voltage under 450 000 contact-separation cycles. Output voltage shows an almost linear relationship with pressure, which has a sensitivity of 11.04 V mm Hg^{-1} ($R^2 = 99.3\%$). Degradation test results indicate that output signals can maintain over 4 days, and full degradation takes over 2 months. Due to the presence of CS, BTS demonstrates antibacterial properties and excellent biocompatibility, which are essential to avoid side effects after implantation. To compare the sensor properties of the BTS and commercial sensors, in small animal experiments, the BTS is implanted under the abdominal cavity skin and a commercial mechanical sensor is placed on the skin as a reference, respectively. Dyspnea causes the thorax to decrease but increases the amplitude of each breath. Therefore, the BTS receives compression force to generate voltage signals. Before damaging the encapsulation layer, the BTS detects activities over 5 days. In large animal experiments, the BTS attaches to the vascular wall, and the commercial sensor inserts into a blood vessel. The contact-separation process occurs during the systole and diastole blood pressure phase. The systolic phase dilates blood vessels creating the BTS contact phase, and the diastolic phase contracts blood vessels making the BTS separation phase. The BTS detects blood pressure changes by inflating and deflating the balloon that is inserted into the blood vessel.

7. Conclusion and Future Perspectives

This review highlights advances in wearable and implantable bioresorbable medical devices, focusing on material options, dissolution process, and device applications. Bioresorbable polymers dissolve into water through hydrolysis processes, with some utilizing additional mechanisms such as mechanical stress, oxidations, or enzymatic reactions. Among these, PLGA emerges as one of the most promising polymers for bioresorbable electronics, owing to its tunable degradation rate, mechanical reliability, and established clinical biocompatibility. The metal oxides further degrade through chemical reaction with NaCl, producing water-soluble compounds. These materials safely dissolve after use, thereby reducing both retrieval surgery risks and e-waste. Such advantages enable applications in skin-interfaced stimulators, energy harvesters, implantable transistors, and sensing devices.

Further enhancing the power efficiency and sensor sensitivity remains a key challenge for bioresorbable devices relative to non-bioresorbable alternatives. The b-WPUE's $\rm d_{33}^{[2]}$ remains 10–100 times lower than non-bioresorbable materials, such as



www.advelectronicmat.de

Pb(Mg_{1/3}Nb_{2/3})O₃-PbTiO₃ (PMN-PT), PZT, and KNN, [^{136–138}] resulting in limited power transfer efficiency. Similarly, capacitive and gelatine-based pressure sensors demonstrate several to 10 times lower sensitivity compared to non-bioresorbable sensors based on poly(vinylidene fluoride) (PVDF, [^{139,140}] PDMS, [^{141,142}] and PEDOT:PSS. [¹⁴³] Enhanced polarization techniques, novel bioresorbable materials, and innovative microstructural designs could address these limitations.

Complete bioresorption of all device components represents another research opportunity. Current bioresorbable devices often incorporate non-bioresorbable conductive materials, [3, 8, 37–39] adhesives, [8,12] and ISF sampling pads. [15] Mg, Fe, gelatine methacryloyl, and PLA are promising bioresorbable alternatives. Future research should focus on ensuring long-term signal fidelity under dynamic biological conditions using these materials. Additionally, bioresorbable sensors typically require nonbioresorbable wireless communication technologies, such as BLE.[10] Potential solutions include measurement techniques that eliminate direct data transmission requirements, such as fluorescence-based detection[14,16] and LC resonant frequency monitoring^[43] or fully bioresorbable wireless communication circuits using bioresorbable transistors and diodes.[44] These approaches would enable truly transient sensing systems with robust data collection capabilities.

Recent advancements in bioresorbable transistor systems, such as Si NM-based MOSFETs and PEDOT:PSS-based OECTs, have demonstrated the potential for transient neural interfaces. [43,134,135] However, improvements in degradation control, signal stability, and wireless power strategies (e.g., LC circuits) are required for long-term operation and implantation. Similarly, bioresorbable implantable sensors face challenges due to the rapid degradation of critical components such as Si-based photodetectors, Zn electrodes, and Mg-based coils limiting their suitability for continuous monitoring and signal fidelity. [42,43,134,135] To address these issues, future research should focus on advanced encapsulation technologies, conductive nanostructures, and comprehensive biocompatibility and safety assessments to enable successful translation into clinical practice. [136]

Ethical considerations such as data privacy, wireless communication security, and patient autonomy are essential for the clinical translation of bioresorbable wireless systems. Despite their growing capabilities, data security measures remain largely absent in current implementations, [1] presenting a clear opportunity for advancement. Incorporating platforms like REDCap^[144] for secure data management, in-sensor encryption (e.g., AES-128), and encrypted wireless protocols (e.g., HTTPS over TLS 1.2 or BLE with AES) can ensure end-to-end data protection. [1] Patient autonomy should be safeguarded through informed consent mechanisms that clearly outline data use, access, and rights.

Ultimately, translating these bioresorbable technologies to medical-grade applications requires design strategies, demonstration protocols, and evaluation procedures that satisfy FDA regulatory requirements.^[145] Such regulatory compliance ensures safe implementation of bioresorbable biomedical systems. Among introduced applications, cardiac stimulator, b-WPUE, and SOP devices demonstrated physiological compatibility during functional periods and resorption processes in rodent implantation studies using three animals each. Although these find-

ings suggest potential viability, larger sample sizes remain necessary to establish statistical significance compared to control groups before advancing to comprehensive preclinical in vivo testing protocols.^[146]

A three-phase technological roadmap envisions the evolution of bioresorbable electronics. In the near term, research will prioritize the enhancement of materials and fabrication techniques to improve power efficiency, sensitivity, and overall performance metrics. The mid-term phase will expand into advanced applications through deeper integration with biological systems, including but not limited to self-reporting diagnostic devices, dissolvable active implants, and adaptive interfaces with living tissues. Long-term innovations will culminate in fully integrated closed-loop medical systems that seamlessly combine sensing capabilities, responsive stimulation, and targeted therapeutic functions, all powered by bioresorbable energy harvesting and secure wireless communication systems that safely dissolve after completing their therapeutic mission.

Acknowledgements

D.Y. P. and H.-M.L. contributed equally to this work. K.K. acknowledges support from the National Research Foundation of Korea (NRF) grant funded by the Korea government (MSIT) (No. RS-2022-NR072054 and RS-2020-NR049568) and support from the Institute of Information & communications Technology Planning & Evaluation (IITP) under the Graduate School of Artificial Intelligence Semiconductor (IITP-2025-RS-2023-00256472) grant funded by the Korea government (MSIT). H.R. acknowledges support from the Technology Innovation Program (20025736, Development of MICS SoC and Platform for In Vivo Implantable Electroceutical Devices) funded By the Ministry of Trade, Industry & Energy (MOTIE, South Korea), and the Nano & Material Technology Development Program through the National Research Foundation of Korea (NRF) funded by Ministry of Science and ICT (RS-2024-00451318).

Conflict of Interest

The authors declare no conflict of interest.

Keywords

actuators, bioresorbable materials, energy harvesters, implantable devices, sensors, skin-interfaced platforms

Received: December 31, 2024 Revised: May 14, 2025 Published online: June 27, 2025

- [1] Y. S. Choi, H. Jeong, R. T. Yin, R. Avila, A. Pfenniger, J. Yoo, J. Y. Lee, A. Tzavelis, Y. J. Lee, S. W. Chen, H. S. Knight, S. Kim, H.-Y. Ahn, G. Wickerson, A. Vázquez-Guardado, E. Higbee-Dempsey, B. A. Russo, M. A. Napolitano, T. J. Holleran, L. A. Razzak, A. N. Miniovich, G. Lee, B. Geist, B. Kim, S. Han, J. A. Brennan, K. Aras, S. S. Kwak, J. Kim, E. A. Waters, et al., Science 2022, 376, 1006.
- [2] H. Xue, J. Jin, Z. Tan, K. Chen, G. Lu, Y. Zeng, X. Hu, X. Peng, L. Jiang, J. Wu, Sci. Adv. 2024, 10, 0260.
- [3] Y. Xu, G. Zhao, L. Zhu, Q. Fei, Z. Zhang, Z. Chen, F. An, Y. Chen, Y. Ling, P. Guo, S. Ding, G. Huang, P.-Y. Chen, Q. Cao, Z. Yan, Proc. Natl. Acad. Sci. USA 2020, 117, 18292.

ADVANCED SCIENCE NEWS

www.advancedsciencenews.com



www.advelectronicmat.de

[32] F. Yang, J. Li, Y. Long, Z. Zhang, L. Wang, J. Sui, Y. Dong, Y. Wang, R. Taylor, D. Ni, W. Cai, P. Wang, T. Hacker, X. Wang, *Science* 2021, 373, 337.

- [33] N. Sezer, M. Koç, Nano Energy 2021, 80, 105567.
- [34] W.-G. Kim, D.-W. Kim, I.-W. Tcho, J.-K. Kim, M.-S. Kim, Y.-K. Choi, ACS Nano 2021, 15, 258.
- [35] J. Wen, X. Pan, H. Fu, B. Xu, Matter 2023, 6, 2153.
- [36] A. Iqbal, P. R. Sura, M. Al-Hasan, I. B. Mabrouk, T. A. Denidni, Sci. Rep. 2022, 12, 13689.
- [37] Y. Li, S. Chen, H. Yan, H. Jiang, J. Luo, C. Zhang, Y. Pang, Y. Tan, Chem. Eng. J. 2023, 468, 143572.
- [38] H. Gong, Z. Xu, Y. Yang, Q. Xu, X. Li, X. Cheng, Y. Huang, F. Zhang, J. Zhao, S. Li, X. Liu, Q. Huang, W. Guo, *Biosens. Bioelectron.* 2020, 169, 112567.
- [39] X. Peng, K. Dong, Y. Zhang, L. Wang, C. Wei, T. Lv, Z. L. Wang, Z. Wu, Adv. Funct. Mater. 2022, 32, 2112241.
- [40] H. Moon, J. Kwon, J. Eun, C. K. Chung, J. S. Kim, N. Chou, S. Kim, Adv. Mater. Technol. 2024, 9, 2301692.
- [41] M. Wu, K. Yao, N. Huang, H. Li, J. Zhou, R. Shi, J. Li, X. Huang, J. Li, H. Jia, Z. Gao, T. H. Wong, D. Li, S. Hou, Y. Liu, S. Zhang, E. Song, I. Yu, X. Yu, Adv. Sci. 2023, 10, 2300504.
- [42] S.-K. Kang, R. K. J. Murphy, S.-W. Hwang, S. M. Lee, D. V. Harburg, N. A. Krueger, J. Shin, P. Gamble, H. Cheng, S. Yu, Z. Liu, J. G. McCall, M. Stephen, H. Ying, J. Kim, G. Park, R. C. Webb, C. H. Lee, S. Chung, D. S. Wie, A. D. Gujar, B. Vemulapalli, A. H. Kim, K.-M. Lee, J. Cheng, Y. Huang, S. H. Lee, P. V. Braun, W. Z. Ray, J. A. Rogers, *Nature* 2016, 530. 71.
- [43] Q. Yang, Z. Hu, M.-H. Seo, Y. Xu, Y. Yan, Y.-H. Hsu, J. Berkovich, K. Lee, T.-L. Liu, S. McDonald, H. Nie, H. Oh, M. Wu, J.-T. Kim, S. A. Miller, Y. Jia, S. Butun, W. Bai, H. Guo, J. Choi, A. Banks, W. Z. Ray, Y. Kozorovitskiy, M. L. Becker, M. A. Pet, M. R. MacEwan, J.-K. Chang, H. Wang, Y. Huang, J. A. Rogers, *Nat. Commun.* 2022, *13*, 6518.
- [44] S.-W. Hwang, H. Tao, D.-H. Kim, H. Cheng, J.-K. Song, E. Rill, M. A. Brenckle, B. Panilaitis, S. M. Won, Y.-S. Kim, Y. M. Song, K. J. Yu, A. Ameen, R. Li, Y. Su, M. Yang, D. L. Kaplan, M. R. Zakin, M. J. Slepian, Y. Huang, F. G. Omenetto, J. A. Rogers, *Science* 2012, 337, 1640.
- [45] S.-W. Hwang, D.-H. Kim, H. Tao, T. Kim, S. Kim, K. J. Yu, B. Panilaitis, J.-W. Jeong, J.-K. Song, F. G. Omenetto, J. A. Rogers, Adv. Funct. Mater. 2013, 23, 4087.
- [46] M. Dobrzyńska-Mizera, J. M. Dodda, X. Liu, M. Knitter, R. N. Oosterbeek, P. Salinas, E. Pozo, A. M. Ferreira, E. R. Sadiku, Adv. Healthcare Mater. 2024, 13, 2401674.
- [47] D. Harpaz, T. Axelrod, A. L. Yitian, E. Eltzov, R. S. Marks, A. I. Y. Tok, Materials 2019, 12, 343.
- [48] L. Chaigneau, A. Perrot, D. Brezulier, J.-F. Coulon, F. Chevire, R. Lebullenger, J. Mech. Behav. Biomed. Mater. 2023, 138, 105571.
- [49] Y. J. Low, A. Andriyana, B. C. Ang, N. I. Zainal Abidin, *Polym. Eng. Sci.* 2020, 60, 2657.
- [50] E. Archer, M. Torretti, S. Madbouly, Phys. Sci. Rev. 2023, 8, 4391.
- [51] A. Basu, A. J. Domb, Adv. Mater. 2018, 30, 1706815.
- [52] L. Wan, L. Lu, T. Zhu, Z. Liu, R. Du, Q. Luo, Q. Xu, Q. Zhang, X. Jia, Biomacromolecules 2022, 23, 4268.
- [53] H. Tsuji, Y. Yamamura, T. Ono, T. Saeki, H. Daimon, K. Fujie, *Macro-mol. React. Eng.* 2008, 2, 522.
- [54] H. Wang, X. Liu, D. E. Christiansen, S. Fattahpour, K. Wang, H. Song, S. Mehraeen, G. Cheng, *Biomater. Sci.* 2021, *9*, 1381.
- [55] S. Y. H. Abdalkarim, H.-Y. Yu, M.-L. Song, Y. Zhou, J. Yao, Q.-Q. Ni, *Carbohydr. Polym.* 2017, 176, 38.
 [56] M. Salomez, M. George, P. Fabre, F. Touchaleaume, G. Cesar, A.
- Lajarrige, E. Gastaldi, *Polym. Degrad. Stab.* **2019**, *167*, 102. [57] M. B. Browning, S. N. Cereceres, P. T. Luong, E. M. Cosgriff-
- Hernandez, J. Biomed. Mater. Res., Part A 2014, 102, 4244. [58] Y. Wang, G. A. Ameer, B. J. Sheppard, R. Langer, Nat. Biotechnol.
- [58] Y. Wang, G. A. Ameer, B. J. Sheppard, R. Langer, *Nat. Biotechnol.* 2002, 20, 602.

- [4] X. Liu, B. Cui, X. Wang, M. Zheng, Z. Bai, O. Yue, Y. Fei, H. Jiang, Adv. Healthcare Mater. 2023, 12, 2202971.
- [5] Y. Wang, Z. Chen, B. Davis, W. Lipman, S. Xing, L. Zhang, T. Wang, P. Hafiz, W. Xie, Z. Yan, Z. Huang, J. Song, W. Bai, *Nat. Commun.* 2024, 15, 511.
- [6] C. Chiappini, E. De Rosa, J. O. Martinez, X. Liu, J. Steele, M. M. Stevens, E. Tasciotti, Nat. Mater. 2015, 14, 532.
- [7] C. M. Boutry, A. Nguyen, Q. O. Lawal, A. Chortos, S. Rondeau-Gagné, Z. Bao, Adv. Mater. 2015, 27, 6954.
- [8] M. Zarei, J. H. Kim, J. T. Han, S. G. Lee, Chem. Eng. J. 2023, 470,
- [9] S. Wan, Z. Zhu, K. Yin, S. Su, H. Bi, T. Xu, H. Zhang, Z. Shi, L. He, L. Sun, Small Methods 2018, 2, 1700374.
- [10] H. Ryu, J. W. Song, H. Luan, Y. Sim, S. S. Kwak, H. Jang, Y. J. Jo, H.-J. Yoon, H. Jeong, J. Shin, D. Y. Park, K. Kwon, G. A. Ameer, J. A. Rogers, Adv. Healthcare Mater. 2024, 13, 2302797.
- [11] S. K. Ghosh, J. Park, S. Na, M. P. Kim, H. Ko, Adv. Sci. 2021, 8, 2005010.
- [12] M. Ali, S. M. Hoseyni, R. Das, M. Awais, I. Basdogan, L. Beker, Adv. Mater. Technol. 2023, 8, 2300347.
- [13] G. Ye, D. Song, J. Song, Y. Zhao, N. Liu, Adv. Funct. Mater. 2023, 33, 2303990.
- [14] M. Sang, M. Cho, S. Lim, I. S. Min, Y. Han, C. Lee, J. Shin, K. Yoon, W.-H. Yeo, T. Lee, S. M. Won, Y. Jung, Y. J. Heo, K. J. Yu, Sci. Adv. 2023, 9, 1765
- [15] L. Bao, J. Park, B. Qin, B. Kim, Sci. Rep. 2022, 12, 10693.
- [16] S. Liu, D. S. Yang, S. Wang, H. Luan, Y. Sekine, J. B. Model, A. J. Aranyosi, R. Ghaffari, J. A. Rogers, *EcoMat* 2023, 5, 13270
- [17] S.-Y. Yang, V. Sencadas, S. S. You, N. Z.-X. Jia, S. S. Srinivasan, H.-W. Huang, A. E. Ahmed, J. Y. Liang, G. Traverso, Adv. Funct. Mater. 2021, 31, 2009289.
- [18] S. Fuada, M. Särestöniemi, M. Katz, Int. J. Online Biomed. Eng. (i/OE) 2024, 20, 115.
- [19] D.-M. Lee, M. Kang, I. Hyun, B.-J. Park, H. J. Kim, S. H. Nam, H.-J. Yoon, H. Ryu, H. Park, B.-O. Choi, S.-W. Kim, *Nat. Commun.* 2023, 14, 7315.
- [20] G. Lee, E. Ray, H.-J. Yoon, S. Genovese, Y. S. Choi, M.-K. Lee, S. Şahin, Y. Yan, H.-Y. Ahn, A. J. Bandodkar, J. Kim, M. Park, H. Ryu, S. S. Kwak, Y. H. Jung, A. Odabas, U. Khandpur, W. Z. Ray, M. R. MacEwan, J. A. Rogers, Sci. Adv. 2022, 8, 9169.
- [21] S. Nagaveni, P. Hunasigidad, D. Pathak, A. Dutta, IEEE Trans. Circuits Syst. I. Reg. Papers 2024, 71, 5030.
- [22] J. Ren, Y. Jiang, X. Jin, Z. Yan, W. Tan, Y. Ding, P. Li, S. Li, Corros. Sci. 2024, 240, 112461.
- [23] J. Hwangbo, H. Seo, G. Sim, R. Avila, M. Nair, B. Kim, Y. Choi, Cell Rep. Phys. Sci. 2024, 5, 102099.
- [24] J.-S. Shim, J. A. Rogers, S.-K. Kang, Mater. Sci. Eng., R 2021, 145, 100624
- [25] M. Kang, D.-M. Lee, I. Hyun, N. Rubab, S.-H. Kim, S.-W. Kim, Chem. Rev. 2023, 123, 11559.
- [26] G. Lee, Y. S. Choi, H.-J. Yoon, J. A. Rogers, Matter 2020, 3, 1031.
- [27] W. Tang, Q. Sun, Z. L. Wang, Chem. Rev. 2023, 123, 12105.
- [28] G. Namgoong, W. Park, F. Bien, IEEE Trans. Biomed. Circuits Syst. 2022, 16, 1116.
- [29] E. Venkatragavaraj, B. Satish, P. R. Vinod, M. S. Vijaya, J. Phys. D: Appl. Phys. 2001, 34, 487.
- [30] M. Acosta, N. Novak, V. Rojas, S. Patel, R. Vaish, J. Koruza, G. A. Rossetti Jr., J. Rödel, Appl. Phys. Rev. 2017, 4, 041305.
- [31] M. T. Chorsi, T. T. Le, F. Lin, T. Vinikoor, R. Das, J. F. Stevens, C. Mundrane, J. Park, K. T. M. Tran, Y. Liu, J. Pfund, R. Thompson, W. He, M. Jain, M. D. Morales-Acosta, O. R. Bilal, K. Kazerounian, H. Ilies, T. D. Nguyen, Sci. Adv. 2023, 9, 6075.

www.advelectronicmat.de

- [59] K. Polak-Kraśna, A. R. Abaei, R. N. Shirazi, E. Parle, O. Carroll, W. Ronan, T. J. Vaughan, J. Mech. Behav. Biomed. Mater. 2021, 118, 104409
- [60] H. K. Makadia, S. J. Siegel, Polymers 2011, 3, 1377.
- [61] H. Ryu, M.-H. Seo, J. A. Rogers, Adv. Healthcare Mater. 2021, 10, 2002236.
- [62] Y. Choi, J. Koo, J. A. Rogers, MRS Bull. 2020, 45, 103.
- [63] B. Shi, J. Xu, J. Zou, Y. R. Li, Z. Zhou, K. Liu, Q. Jia, H. B. Jiang, Heliyon 2024, 10, 24348.
- [64] X. Huang, D. Wang, Z. Yuan, W. Xie, Y. Wu, R. Li, Y. Zhao, D. Luo, L. Cen, B. Chen, H. Wu, H. Xu, X. Sheng, M. Zhang, L. Zhao, L. Yin, Small 2018, 14, 1800994.
- [65] Y. K. Lee, K. J. Yu, Y. Kim, Y. Yoon, Z. Xie, E. Song, H. Luan, X. Feng, Y. Huang, J. A. Rogers, ACS Appl. Mater. Interfaces 2017, 9, 42633.
- [66] H. Guo, D. D'Andrea, J. Zhao, Y. Xu, Z. Qiao, L. E. Janes, N. K. Murthy, R. Li, Z. Xie, Z. Song, R. Meda, J. Koo, W. Bai, Y. S. Choi, S. W. Jordan, Y. Huang, C. K. Franz, J. A. Rogers, Adv. Funct. Mater. 2021, 31, 2102724.
- [67] Q. Yang, T. Wei, R. T. Yin, M. Wu, Y. Xu, J. Koo, Y. S. Choi, Z. Xie, S. W. Chen, I. Kandela, S. Yao, Y. Deng, R. Avila, T.-L. Liu, W. Bai, Y. Yang, M. Han, Q. Zhang, C. R. Haney, K. Benjamin Lee, K. Aras, T. Wang, M.-H. Seo, H. Luan, S. M. Lee, A. Brikha, N. Ghoreishi-Haack, L. Tran, I. Stepien, F. Aird, et al., Nat. Mater. 2021, 20, 1559.
- [68] J. W. Song, H. Ryu, W. Bai, Z. Xie, A. Vázquez-Guardado, K. Nandoliya, R. Avila, G. Lee, Z. Song, J. Kim, M.-K. Lee, Y. Liu, M. Kim, H. Wang, Y. Wu, H.-J. Yoon, S. S. Kwak, J. Shin, K. Kwon, W. Lu, X. Chen, Y. Huang, G. A. Ameer, J. A. Rogers, Sci. Adv. 2023, 9, 4687.
- [69] M. Zhao, B. Song, J. Pu, T. Wada, B. Reid, G. Tai, F. Wang, A. Guo, P. Walczysko, Y. Gu, T. Sasaki, A. Suzuki, J. V. Forrester, H. R. Bourne, P. N. Devreotes, C. D. McCaig, J. M. Penninger, *Nature* 2006, 442, 457.
- [70] T. B. Saw, X. Gao, M. Li, J. He, A. P. Le, S. Marsh, K. Lin, A. Ludwig, J. Prost, C. T. Lim, *Nat. Phys.* **2022**, *18*, 1122.
- [71] T. C. Shyu, P. F. Damasceno, P. M. Dodd, A. Lamoureux, L. Xu, M. Shlian, M. Shtein, S. C. Glotzer, N. A. Kotov, *Nat. Mater.* 2015, 14, 785.
- [72] Y. Xu, B. Sun, Y. Ling, Q. Fei, Z. Chen, X. Li, P. Guo, N. Jeon, S. Goswami, Y. Liao, S. Ding, Q. Yu, J. Lin, G. Huang, Z. Yan, *Proc. Natl. Acad. Sci. USA* 2020, 117, 205.
- [73] B. Sun, R. N. McCay, S. Goswami, Y. Xu, C. Zhang, Y. Ling, J. Lin, Z. Yan, Adv. Mater. 2018, 30, 1804327.
- [74] A. Miyamoto, S. Lee, N. F. Cooray, S. Lee, M. Mori, N. Matsuhisa, H. Jin, L. Yoda, T. Yokota, A. Itoh, M. Sekino, H. Kawasaki, T. Ebihara, M. Amagai, T. Someya, Nat. Nanotechnol. 2017, 12, 907.
- [75] S. Chao, Y. Li, R. Zhao, L. Zhang, Y. Li, C. Wang, X. Li, J. Drug Delivery Sci. Technol. 2018, 44, 440.
- [76] R. Neiva, W. V. Giannobile, in *Preprosthetic and Maxillofacial Surgery*, Elsevier, Cambridge, UK, 2011, pp. 305–326.
- [77] J. Aragoneses, A. Suárez, C. Rodríguez, J. M. Aragoneses, Int. J. Environ. Res. Public Health (IJERPH) 2021, 18, 3881.
- [78] M. Gierek, W. Łabuś, D. Kitala, A. Lorek, G. Ochała-Gierek, K. M. Zagórska, D. Waniczek, K. Szyluk, P. Niemiec, *Biomedicines* 2022, 10, 2870.
- [79] Y. Wang, F. Lu, E. Hu, K. Yu, J. Li, R. Bao, F. Dai, G. Lan, R. Xie, ACS Appl. Mater. Interfaces 2021, 13, 16048.
- [80] S. M. Kelleher, O. Habimana, J. Lawler, B. O' Reilly, S. Daniels, E. Casey, A. Cowley, ACS Appl. Mater. Interfaces 2016, 8, 14966.
- [81] H. Shahali, J. Hasan, A. Mathews, H. Wang, C. Yan, T. Tesfamichael, P. K. D. V. Yarlagadda, J. Mater. Chem. B 2019, 7, 1300.
- [82] D.-N. Phan, N. Dorjjugder, Y. Saito, M. Q. Khan, A. Ullah, X. Bie, G. Taguchi, I.-S. Kim, Mater. Today Commun. 2020, 25, 101377.
- [83] Y. Liu, N. Nie, H. Tang, C. Zhang, K. Chen, W. Wang, J. Liu, ACS Appl. Mater. Interfaces 2021, 13, 11631.

- [84] R. Liu, Y. Tang, H. Liu, L. Zeng, Z. Ma, J. Li, Y. Zhao, L. Ren, K. Yang, J. Mater. Sci. Technol. 2020, 47, 202.
- [85] H. Keles, A. Naylor, F. Clegg, C. Sammon, Polym. Degrad. Stab. 2015, 119, 228.
- [86] S.-W. Han, C. Nakamura, N. Kotobuki, I. Obataya, H. Ohgushi, T. Nagamune, J. Miyake, Nanomedicine: Nanotechnol. Biol. Med. 2008, 4 215
- [87] S. H. C. Anderson, H. Elliott, D. J. Wallis, L. T. Canham, J. J. Powell, Phys. Status Solidi 2003, 197, 331.
- [88] N. Shaari, S. K. Kamarudin, S. Basri, L. K. Shyuan, M. S. Masdar, D. Nordin, J. Appl. Polym. Sci. 2018, 135, 46666.
- [89] C. Gao, E. Pollet, L. Avérous, Food Hydrocolloids 2017, 63, 414.
- [90] D.-H. Kim, N. Lu, R. Ma, Y.-S. Kim, R.-H. Kim, S. Wang, J. Wu, S. M. Won, H. Tao, A. Islam, K. J. Yu, T. Kim, R. Chowdhury, M. Ying, L. Xu, M. Li, H.-J. Chung, H. Keum, M. McCormick, P. Liu, Y.-W. Zhang, F. G. Omenetto, Y. Huang, T. Coleman, J. A. Rogers, *Science* 2011, 333, 838.
- [91] Y. Han, Y. Han, X. Zhang, L. Li, C. Zhang, J. Liu, G. Lu, H.-D. Yu, W. Huang, ACS Appl. Mater. Interfaces 2020, 12, 16442.
- [92] C. Yang, Y. Huang, H. Cheng, L. Jiang, L. Qu, Adv. Mater. 2019, 31, 1805705.
- [93] T. Xu, X. Ding, Y. Huang, C. Shao, L. Song, X. Gao, Z. Zhang, L. Qu, Energy Environ. Sci. 2019, 12, 972.
- [94] R. Shi, D. Chen, Q. Liu, Y. Wu, X. Xu, L. Zhang, W. Tian, Int. J. Mol. Sci. 2009, 10, 4223.
- [95] S. C. B. Mannsfeld, B. C.-K. Tee, R. M. Stoltenberg, C. V. H.-H. Chen, S. Barman, B. V. O. Muir, A. N. Sokolov, C. Reese, Z. Bao, *Nat. Mater.* 2010, 9, 859.
- [96] G. Schwartz, B. C.-K. Tee, J. Mei, A. L. Appleton, D. H. Kim, H. Wang, Z. Bao, Nat. Commun. 2013, 4, 1859.
- [97] B. C.-K. Tee, A. Chortos, R. R. Dunn, G. Schwartz, E. Eason, Z. Bao, Adv. Funct. Mater. 2014, 24, 5427.
- [98] C. W. Pouton, S. Akhtar, Adv. Drug Delivery Rev. 1996, 18, 133.
- [99] X. Li, T. Yang, Y. Yang, J. Zhu, L. Li, F. E. Alam, X. Li, K. Wang, H. Cheng, C.-T. Lin, Y. Fang, H. Zhu, Adv. Funct. Mater. 2016, 26, 1322.
- [100] Y. Park, J. Shim, S. Jeong, G.-R. Yi, H. Chae, J. W. Bae, S. O. Kim, C. Pang, Adv. Mater. 2017, 29, 1606453.
- [101] T. Yamada, Y. Hayamizu, Y. Yamamoto, Y. Yomogida, A. Izadi-Najafabadi, D. N. Futaba, K. Hata, Nat. Nanotechnol. 2011, 6, 296.
- [102] G. Shi, Z. Zhao, J.-H. Pai, I. Lee, L. Zhang, C. Stevenson, K. Ishara, R. Zhang, H. Zhu, J. Ma, Adv. Funct. Mater. 2016, 26, 7614.
- [103] A. Ní Annaidh, K. Bruyère, M. Destrade, M. D. Gilchrist, M. Otténio, I. Mech. Behav. Biomed. Mater. 2012. 5, 139.
- [104] Y. Lee, J. Park, A. Choe, S. Cho, J. Kim, H. Ko, Adv. Funct. Mater. 2020, 30, 1904523.
- [105] Y. Yang, Y. Zhou, J. M. Wu, Z. L. Wang, ACS Nano 2012, 6, 8456.
- [106] D. Y. Park, D. J. Joe, D. H. Kim, H. Park, J. H. Han, C. K. Jeong, H. Park, J. G. Park, B. Joung, K. J. Lee, Adv. Mater. 2017, 29, 1702308.
- [107] K. Roy, S. K. Ghosh, A. Sultana, S. Garain, M. Xie, C. R. Bowen, K. Henkel, D. Schmei β er, D. Mandal, *ACS Appl. Nano Mater.* **2019**, *2*, 2013.
- [108] A. P. Avolio, M. Butlin, A. Walsh, *Physiol. Meas.* **2010**, *31*, R1.
- [109] I. Johnson, H. Liu, PLoS One 2013, 8, 65603.
- [110] W. Nichols, Am. J. Hypertens. 2005, 18, 3.
- [111] S. Munir, B. Jiang, A. Guilcher, S. Brett, S. Redwood, M. Marber, P. Chowienczyk, Am. J. Physiol.: Heart Circ. Physiol. 2008, 294, H1645.
- [112] S. Chen, Y. Hao, W. Cui, J. Chang, Y. Zhou, J. Mater. Sci. 2013, 48, 6567.
- [113] Q. Zhang, L. Zhao, H. Yang, L. Kong, F. Ran, J. Membr. Sci. 2021, 629, 119083.
- [114] L. Yin, L. Fei, F. Cui, C. Tang, C. Yin, Biomaterials 2007, 28, 1258.
- [115] N. Post, D. Eddy, C. Huntley, M. C. I. van Schalkwyk, M. Shrotri, D. Leeman, S. Rigby, S. V. Williams, W. H. Bermingham, P. Kellam, J.





www.advelectronicmat.de

- Maher, A. M. Shields, G. Amirthalingam, S. J. Peacock, S. A. Ismail, *PLoS One* **2020**, *15*, 0244126.
- [116] H. Lee, G. Bonfante, Y. Sasaki, N. Takama, T. Minami, B. Kim, Med. Devices Sens. 2020, 3, 10109.
- [117] K. Takeuchi, N. Takama, R. Kinoshita, T. Okitsu, B. Kim, Biomed. Microdevices 2020, 22, 79.
- [118] K. Takeuchi, N. Takama, K. Sharma, O. Paul, P. Ruther, T. Suga, B. Kim, Drug Delivery Transl. Res. 2022, 12, 435.
- [119] H. Liu, E. Dai, R. Xiao, Z. Zhou, M. Zhang, Z. Bai, Y. Shao, K. Qi, J. Tu, C. Wang, S. Wang, Sens. Actuators, B 2021, 329, 129196.
- [120] M. Seok, S. Yoon, M. Kim, Y.-H. Cho, Nanoscale Adv. 2021, 3, 4843.
- [121] J. Pérez, J. Muñoz-Dorado, T. de la Rubia, J. Martínez, Int. Microbiol. 2002, 5, 53.
- [122] V. M. Pathak, Navneet, Bioresour. Bioprocess. 2017, 4, 15.
- [123] I. Gaytán, M. Burelo, H. Loza-Tavera, Appl. Microbiol. Biotechnol. 2021, 105, 991.
- [124] S. M. Satti, A. A. Shah, Lett. Appl. Microbiol. 2020, 70, 413.
- [125] P. S. Tourinho, C. A. M. van Gestel, S. Lofts, C. Svendsen, A. M. V. M. Soares, S. Loureiro, Environ. Toxicol. Chem. 2012, 31, 1679.
- [126] N. Ghareaghajlou, S. Hallaj-Nezhadi, Z. Ghasempour, Food Chem. 2021, 365, 130482.
- [127] K. Marszałek, Ł. Woźniak, B. Kruszewski, S. Skąpska, Int. J. Mol. Sci. 2017, 18, 277.
- [128] G. Mabilleau, M. F. Moreau, R. Filmon, M. F. Baslé, D. Chappard, Biomaterials 2004, 25, 5155.
- [129] J. H. Song, R. J. Murphy, R. Narayan, G. B. H. Davies, *Philos. Trans. R. Soc.*, B 2009, 364, 2127.
- [130] S.-K. Kang, J. Koo, Y. K. Lee, J. A. Rogers, Acc. Chem. Res. 2018, 51,
- [131] K. Liu, B. Ouyang, X. Guo, Y. Guo, Y. Liu, npj Flexible Electron. 2022, 6. 1.
- [132] Z. Liu, T. Li, S. Li, C. C. Mi, Nexus 2024, 1, 100014.
- [133] K. J. Yu, D. Kuzum, S.-W. Hwang, B. H. Kim, H. Juul, N. H. Kim, S. M. Won, K. Chiang, M. Trumpis, A. G. Richardson, H. Cheng, H. Fang, M. Thompson, H. Bink, D. Talos, K. J. Seo, H. N. Lee, S.-K. Kang, J.-H. Kim, J. Y. Lee, Y. Huang, F. E. Jensen, M. A. Dichter, T. H. Lucas, J. Viventi, B. Litt, J. A. Rogers, Nat. Mater. 2016, 15, 782.

- [134] W. Bai, J. Shin, R. Fu, I. Kandela, D. Lu, X. Ni, Y. Park, Z. Liu, T. Hang, D. Wu, Y. Liu, C. R. Haney, I. Stepien, Q. Yang, J. Zhao, K. R. Nandoliya, H. Zhang, X. Sheng, L. Yin, K. MacRenaris, A. Brikha, F. Aird, M. Pezhouh, J. Hornick, W. Zhou, J. A. Rogers, *Nat. Biomed. Eng.* 2019, 3, 644.
- [135] H. Ouyang, Z. Li, M. Gu, Y. Hu, L. Xu, D. Jiang, S. Cheng, Y. Zou, Y. Deng, B. Shi, W. Hua, Y. Fan, Z. Li, Z. Wang, Adv. Mater. 2021, 33, 2102302.
- [136] T. Zhang, H. Liang, Z. Wang, C. Qiu, Y. B. Peng, X. Zhu, J. Li, X. Ge, J. Xu, X. Huang, J. Tong, J. Ou-Yang, X. Yang, F. Li, B. Zhu, Sci. Adv. 2022. 8, 0159.
- [137] L. Shi, P. Wu, L. Yu, Y. Zhao, Z. Li, W. Zhao, Z. Wang, Y. Peng, W. Hua, J. Wang, R. Song, W. Fei, *Ceram. Int.* 2022, 48, 10024.
- [138] L. Jiang, B. Wu, X. Wei, X. Lv, H. Xue, G. Lu, Y. Zeng, J. Xing, W. Wu, J. Wu, Mater. Horiz. 2022, 9, 2180.
- [139] W. Deng, Nano Energy 2019, 55, 516
- [140] L. Lu, N. Zhao, J. Liu, B. Yang, J. Mater. Chem. C 2021, 9, 9309.
- [141] L. Singh, M. Bhattacharjee, IEEE J. Flex. Electron. 2023, 2, 77.
- [142] B. Zhu, Z. Niu, H. Wang, W. R. Leow, H. Wang, Y. Li, L. Zheng, J. Wei, F. Huo, X. Chen, Small 2014, 10, 3625.
- [143] A. Krishnan, S. Das, M. Bhattacharjee, IEEE J. Flex. Electron. 2023, 2, 350
- [144] P. A. Harris, R. Taylor, B. L. Minor, V. Elliott, M. Fernandez, L. O'Neal, L. McLeod, G. Delacqua, F. Delacqua, J. Kirby, S. N. Duda, J. Biomed. Inf. 2019, 95, 103208.
- [145] in ANSI/AAMI/ISO 10993-1:2018; Biological Evaluation of Medical Devices—Part 1: Evaluation and Testing within a Risk Management Process, AAMI, Arlington, VA, USA, 2020
- [146] Center for Devices and Radiological Health, General Considerations for Animal Studies Intended to Evaluate Medical Devices, U.S. Food and Drug Administration, 2023, https://www.fda.gov/regulatory-information/search-fda-guidance-documents/general-considerations-animal-studies-intended-evaluate-medical-devices (accessed: May 2025).



Do Yun Park received his B.S. degree in electrical engineering from the Korea Advanced Institute of Science and Technology (KAIST) in Daejeon, South Korea, in 2022. He received his M.S. degree in electrical engineering from the KAIST in 2024. He is currently pursuing his Ph.D. degree in Graduate School of Artificial Intelligence Semiconductor at KAIST. His current research interests include embedded systems and bioelectronics.

2199160x, 2025, 10, Downloaded from https://advanced.onlinelibrary.wiley.com/doi/10.1002/aclm.202400997 by Chung-Ang University, Seoul, Wiley Online Library on [06/07/2025]. See the Terms and Conditions (https://onlinelibrary.wiley.com/terms

and-conditions) on Wiley Online Library for rules of use; OA articles are governed by the applicable Creative Commons



Hye-Min Lee is a third-year student in advanced materials engineering at Chung-Ang University. Since 2023, she has been an undergraduate researcher in the Transformable Electronics & Energy Solution Lab, led by Prof. Hanjun Ryu. Her research interests include bioresorbable materials and bioresorbable electrical stimulators for chronic wound healing.



Su-Hwan Kim received the B.S. degree (2022) in electrical engineering from the Ulsan National Institute of Science and Technology (UNIST), Ulsan, South Korea, and the M.S. degree (2024) in electrical engineering from the Korea Advanced Institute of Science and Technology (KAIST), Daejeon, South Korea. Since 2024, He is currently pursuing the Ph.D. degree in Electrical Engineering, KAIST. His current research interests include energy harvesting system, biomedical system, wireless power transfer system, and its applications.



Youngmin Sim received the B.S. degree in electrical engineering from the Korea Advanced Institute of Science and Technology (KAIST), Daejeon, South Korea, in 2021. He is currently pursuing the integrated M.S. and Ph.D. degree in electrical engineering, KAIST. His current research interests include biomedical system, wearable AI system, and its applications.



Yoojin Kang received dual B.S. degrees (2023) in biomedical engineering and earth resources and environmental engineering from Hanyang University, Seoul, South Korea. She is currently pursuing her M.S. degree in electrical engineering at Koran Advanced Institute of Science and Technology (KAIST), Daejeon, South Korea, with expected graduation in 2025. Her research interests focus on the development of wearable systems for biomedical monitoring, including capnography.



Gyu-rim Jang received the M.S. degree (2022) in electrical engineering from the Daegu Gyeongbuk Institute of Science and Technology (DGIST), Daegu, South Korea. Since 2022, she has been pursuing the M.S. degree in electrical engineering at the Korea Advanced Institute of Science and Technology (KAIST), Daejeon, South Korea. Her current research interests include biomedical systems, environmental monitoring, energy harvesting systems, and related applications.



Sara Kim received the B.S. degree (2016) in electrical and computer engineering from Worcester Polytechnic Institute (WPI), Worcester, USA, and the M.S. degree (2024) in electrical engineering from the Korea Advanced Institute of Science and Technology (KAIST), Daejeon, South Korea. She is currently pursuing the Ph.D. degree in electrical engineering in KAIST. Her current research interests include high speed wireline and optical transceivers.



Kyeongha Kwon received the Ph.D. degree in electrical engineering from the Korea Advanced Institute of Science and Technology (KAIST), Daejeon, South Korea, in 2018. From 2018 to 2020, she was with the Center for Bio-integrated Electronics (CBIE) at Northwestern University, IL, USA, as a post-doctoral researcher. Since 2020, she has been with the Faculty of Electrical Engineering, KAIST, where she is currently an associate professor. Her research interests span a wide range of topics in wireline communication, bioelectronics, and battery management system.



Hanjun Ryu is an assistant professor of the Department of Advanced Materials Engineering at Chung-Ang University. His group is developing nanogenerators for energy solutions, bioresorbable biomedical electronics for wound management, and shape transformable 3D flexible electronics for brain organoid—machine interface. He received his Ph.D. degree in material science from Sungkyunkwan University in 2019. From 2019 to 2022 he was on the postdoctoral researcher at Northwestern University.